Politecnico di Torino
Master of Science in Aerospace Engineering

Data-driven reduced order models of sloshing in horizontal cylindrical tanks

In collaboration with the
von Karman Institute for Fluid Dynamics

Supervisors:

Prof. Domenic D'AMBROSIO

Prof. Miguel A. MENDEZ

Ph.D. Pedro A. MARQUES

Eng. Samuel AHIZI

Student:

Tommaso DE MARIA

Academic Year 2023/2024

Le vent se lève! . . .
il faut tenter de vivre!

Paul Valéry

Acknowledgments / Ringraziamenti

Special thanks to my supervisors at the von Karman Institute for Fluid Dynamics. Prof. Miguel Mendez who in this months has given me the thrill of working in an academic team, After each meeting I felt super motivated.
Thanks to PhD Pedro Marques, very nice person, who from day one was very kind and helpful with me.
Thanks to Eng. Samuel Ahizi who gave me a lot of help and ideas to build this work.

Thanks to the STP "international" team, so international that if we compute the barycentre considering each STP it should be near Bari. The atmosphere that was established reflected a typical high school class, creating a comfortable climate. Completely different personalities united by 'BANG'.
(Thanks also to my last house-mates, now "very good" experts on sloshing)

Grazie alla mia famiglia, a mio padre che mi ha sempre spronato a fare quello che meglio credevo, e a mia madre che ogni sera si ostina a chiamarmi allo stesso orario (e ogni sera non rispondo perché non ha ancora capito che a quell'ora ceno) e chiaramente la videochiamata della domenica dopo pranzo.

Vita da fuorisede: Tornare a casa un mese l'anno e ritrovare la stessa atmosfera non è scontato. Ai miei amici diggiù che ogni volta che scendo a mi fanno sentire come se non fossi mai andato.

Ringraziamento ai miei colleghi del PoliTo conosciuti in questi anni a chi mi ha aiutato (sopratutto in questo semestre), e ai miei colleghi di Icarus a cui auguro di costruire il miglior UAV solar-powered della storia.

Tornare al *Mar*e dona molta *Gio*ia,
*Gia*cere sulla sabbia *Lav*a via i pensieri.

Abstract

The use of alternative fuels for future aerial or naval mobility poses several challenges, particularly for liquid fuels such as cryogenic hydrogen. When stored in reservoirs and subjected to external excitation, they experience sloshing, the movement of the free surface. This phenomenon is particularly critical from both an inertial perspective, as forces are exerted on the tank walls, and from a thermodynamic perspective, as cryogenic liquids suffer phase changes, leading to fluctuations in gas pressure inside the tank. Investigating these phenomena and understanding their underlying dynamics is essential for developing diagnostic tools and creating a digital twin, enabling control techniques to be implemented to manage these fluctuations and optimize them for our purposes.

This work aims to investigate the feasibility of identifying a reduced-order model (ROM) of sloshing in horizontal cylindrical tanks. The proposed approach is to identify the model from 2D computational fluid dynamics (CFD) simulations in OpenFOAM. The relevant testing conditions were selected from the scaling of the problem according to the relevant non-dimensional numbers. Then, the closure terms of the ROM are identified from the numerical database through a data-driven inverse method.
This approach requires a non-linear optimization step to minimize the deviations between the model predictions and high-fidelity CFD, while the ROM's closure terms are expressed via parametric functions with varying degrees of complexity. As a major outcome of this work, we assess the performance of such functions for the most relevant sloshing condition.

Contents

1 Introduction **2**

1.1 Framework 2

1.2 Motivation and objectives 4

1.3 Thesis outline 5

2 Theoretical Background **6**

2.1 Sloshing dynamics 6

2.1.1 Governing equations 7

2.1.2 Sloshing regimes 8

2.2 Linear sloshing potential flow 9

2.2.1 Potential solution for half filled tank 10

2.2.2 Natural frequencies and sloshing masses 12

2.3 Equivalent mechanical model 13

2.4 ROM formulation 14

3 Nondimensionalization and Scaling **16**

3.1 Dimensionless numbers 17

3.2 Scaling similarity 18

3.2.1 Geometry similarity 18

3.2.2 Kinematic similarity 19

3.2.3 Dynamic Similarity 19

4 Numerical simulations for lateral sloshing 21

4.1 Numerical set-up 21

4.1.1 Volume of Fluids 22

4.1.2 interFoam solver 23

4.2 Forcing application 24

4.2.1 Dynamic Mesh 25

4.2.2 Time-dependent acceleration 25

4.3 Simulation outputs 26

4.3.1 Simulation strategy comparison 28

4.4 Grid convergence study 31

5 Reduced-order model calibration 36

5.1 Cost Function 36

5.2 Optimization algorithms 38

5.3 Optimization with multiple simulations 39

6 Results 40

6.1 Sloshing regime identification 41

6.1.1 Wave height at fixed point 41

6.1.2 Centre of gravity 44

6.1.3 Phase plane plot 48

6.2 Damping evaluation 51

6.2.1 Performance of the potential flow model 51

6.2.2 Performance of the mechanical model 52

6.2.3 Comparison between the two models 59

7 Conclusions **63**

7.1 Future work 63

A OpenFoam algorithms **66**

A.1 Modified interFoam solver 68

List of Figures

1.1 Liquid sloshing 3

1.2 Sloshing inside a truck tank 4

2.1 Half filled horizontal cylinder [1] 6

2.2 Visualisation of sloshing regimes in a vertical cylinder [2]. 8

2.3 Sloshing regimes for upright cylinders 9

2.4 Sloshing mechanical model 13

3.1 Hydrodinamic regimes [3] 20

4.1 Volume of Fluids approach 22

4.2 Half filled cylinder 23

4.3 Probe location 27

4.4 Pressure x-direction 28

4.5 Centre of Gravity in rest conditions 29

4.6 Dynamic mesh vs. acceleration 29

4.7 Dynamic mesh vs. acceleration: Envelope 30

4.8 Calculation Time 30

4.9 Simulation comparison without Boundary Layer 32

4.10 very Coarse mesh 33

4.11 Middle mesh 33

4.12 Fine mesh 33
4.13 Grid refinement study in free damping 34
4.14 Grids refinement 35
4.15 Grids refinement study 35

5.1 Peaks envelope 38

6.1 Simulation matrix 40
6.2 Free surface position 42
6.3 Surface height planar simulation 43
6.4 Surface height chaotic simulation 43
6.5 STFT applied to the surface height time-series. 43
6.6 Centre of gravity displacement x-direction planar simulation 44
6.7 Centre of gravity displacement y-direction planar simulation 44
6.8 Wave breaking $t = \bar{t}$ 45
6.9 Wave breaking $t = \bar{t} + \Delta t$ 46
6.10 Centre of gravity displacement x-direction chaotic simulation 46
6.11 Centre of gravity displacement y-direction chaotic simulation 46
6.12 Closeup CG chaotic regime 47
6.13 Phase plane plot Sim no. 42 49
6.14 Phase plane plot Sim no. 53 49
6.15 Phase plane plots 49
6.16 Regime Identification by circular score 50
6.17 Regime Identification 50
6.18 Optimization with potential solution 52
6.19 Envelope of surface height 53
6.20 Constant damping ROM 53

6.21 Overall cost function 54
6.22 Cost function of each simulation 55
6.23 Envelope Reassessment of simulation with the new parameters . . . 55
6.24 Reassessment of simulation with the new parameters 56
6.25 Multiple restarts 56
6.26 Overall cost function 57
6.27 Cost function of each simulation 58
6.28 Envelope of the simulation no. 42 58
6.29 Variable damping 59
6.30 Comparison between the two models 60
6.31 Envelope of surface height simulations ID 10 and 42 61
6.32 Envelope of surface height simulation ID 87 62

List of Tables

2.1 Natural frequency half filled tank 12

2.2 Sloshing masses from potential theory 13

3.1 Reference quantites for scaling 17

3.2 Simulation matrix 18

4.1 Simulation phases 22

4.2 Simulation set-up values 24

4.3 Damping coefficient in free damping 34

4.4 Grid studies 34

6.1 ROM compared 60

6.2 ROM extended to chaotic cases 61

Nomenclature

Greek symbols

α	Relative fluid phase
β_i	Regime differentiation parameter (Miles)
δ	Damping factor
η	Displacement of free surface
κ	Volume curvature
ν	Viscosity
Ω	Forcing frequency
ω_i	i-th natural frequency
Ψ	Spatial function
ρ	Density
Σ	Free surface area
σ	Surface tension
τ	Simulation time parameter
τ	Viscous stress
τ_t	Turbulent stress
θ	Angular coordinate
ζ	Damping coefficient
Co	Courant number

Latin symbols

(x, y, z)	Spatial coordinates

$[K]$	Potential stiffness matrix
$[M]$	Potential Mass matrix
$[N]$	Spatial function matrix
$\bar{r}$	Radius of wave height evaluation
g	Gravity acceleration
g_σ	Surface tension
J	Cost function
k	Spring coefficient
L	Cylinder length
p	Pressure
q_i	Potential solution coefficient
R	Cylinder radius
r	Radial coordinate
T	Torque
t	Time
u_i	Fluid velocity
V	Fluid volume
X	Tank displacement
X_0	Forcing amplitude
x_i	Displacement of the i-th mass
AR	Grid refinement parameter
Fr	Froude number
Re	Reynolds number

Operators

$\frac{\partial \bullet}{\partial \bullet}$	Partial derivative
$\bar{\bullet}$	Reference quantity
$\bullet^*$	Non-Dimensional quantity
$\dot{\bullet}$	Time-derivation

$\nabla(\bullet)$ Gradient

$\nabla \cdot (\bullet)$ Divergence

$\nabla^2(\bullet)$ Laplacian

Vectors

$\mathbf{\Phi}$ Potential function

$\mathbf{f}$ Fluid acceleration

$\mathbf{u}$ Fluid velocity

Chapter 1

Introduction

1.1 Framework

The physical phenomenon investigated in this thesis is sloshing. Formally, this can be defined as the movement of liquid inside a tank[4]. Sloshing is easily experienced in everyday life, for example, when we take a hot cup of tea and with involuntary movements swing the surface from side to side of the cup with the risk of burning ourselves.
Some examples are reported in figure 1.1

Studies on sloshing began in the 1960s [6] through the National Aeronautics and Space Administration (NASA) for applications on space launchers. These works were finalized after some space vehicle failures caused by sloshing, such as the missile Jupiter IRBM fired from Cape Canaveral by NASA in 1957[7].

In 1984 Miles[8, 9] developed a theoretical study of the effects of a liquid subjected to external forcing deriving the principal regimes. Ibrahim [4], in 2005, reviewed the research work developed on sloshing both from a theoretical point of view and for engineering applications. In addition to the transport part, and in particular spacecraft, the phenomenon also affects terrestrial structures, of which nuclear rectors are of considerable study.
From Apollo 11 (1969)[10] to Falcon 1 (2007)[11], propellant sloshing can still cause instabilities in pitch, roll and yaw, and for that failures occur.

Sloshing is a phenomenon in which a liquid inside a partially filled is subject to external excitations which trigger its motion. This latter excitation will set in motion the surface of the liquid in contact with the gas, which through waves will oscillate from one wall of the cylinder to the other.
The response of the liquid to excitation depends not only on the amplitude of the oscillation but also on the frequency. The closer the imposed frequency is to the resonance frequency of the tank, the more the movement of the liquid will no

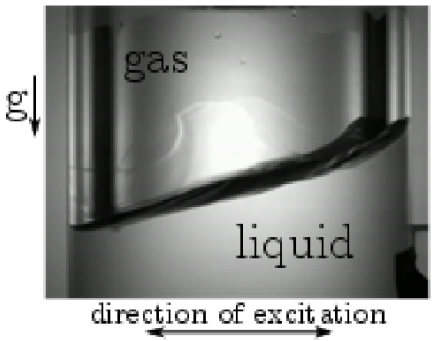

(a) Experimental investigation on sloshing [2]

(b) Sloshing in a cup of coffee[5]

Figure 1.1: Liquid sloshing

longer be planar. Non-linear characters will begin to be present which makes the regime of movement chaotic with waves jumping and falling.

The theory for vertical cylinders developed over the past 60 years does not see as much development in detail for horizontal cylinders that are investigated in this study.
However, more recently, the interest in this application has risen, especially in the transportation sector (i.e., naval and aeronautics), since in these types of transportation, the ideal design for the tank develops in the longitudinal direction. In addition to the forces that are discharged on the tank walls, a phenomenon that affects tanks filled with cryogenic propellant is the effect of pressurization[12, 13]. Pressure fluctuation that occurs in sloshing, causes a pressure variation inside the tank due to the phase change of the cryogenic liquid, and safety valves are used to restore the pressure to a normal condition.The drop/rise is dependent on the boundary conditions of the system, the type of excitation, and the presence of other species in the ullage[14, 15].
Active sloshing control would allow the oscillations to be dampened so that techniques involving loss of propellant such as the relief valves described above would not be necessary[16].

Figure 1.2: Sloshing inside a truck tank

1.2 Motivation and objectives

The purpose of this thesis is to develop a reduced model by using 2-dimensional CFD simulations of the sloshing phenomenon inside a half-filled horizontal tank.

The advantage of constructing this Reduced Order Model (ROM) using CFD data is to obtain results that to a good approximation reproduce those of finite-volume simulations almost instantaneously, in contrast to CFD simulations that require a lot of simulation time to solve.

The challenge is to find the closure terms: the damping term, which describes the loss of mechanical energy from the sloshing waves to the container walls, and the second is the actual mass of liquid which is "excited" due to the forcing motion. These two terms are well accounted for in upright cylinders [17, 18], however such is not the case in horizontal tanks.

From the simulations, we extracted the free surface height at a specific distance from the center of the tank and the pressure distribution along the tank wall. From the fluid height, using both the potential fluid model and a mechanical model, the damping coefficient function is extrapolated and the relative sloshing mass. By entering the amplitude and frequency of the forcing, to find in this way an analogous and alternative solution to CFD. Both the force and the position of the center of gravity were extracted from the pressure probes.

This approach opens up several possibilities for future development. It could be possible to build a digital twin that takes force inputs from sensors, putting them into the model gives the prediction of the center of gravity displacement over time, or wave height movement, and implements behaviors to mitigate or control the liquid motion inside the tank.

1.3 Thesis outline

1. **Chapter 1**: Introduction to sloshing. The problem is defined, motivating the engineering problems and short dissertation on the history, finally defining the objectives.
2. **Chapter 2**: Definition of sloshing regimes, mathematical formulation of the problem using potential theory and mechanical model.
3. **Chapter 3**: Numerical simulation setup. Convergence criteria and grid convergence study.
4. **Chapter 4**: Optimization criteria formulation
5. **Chapter 5**: Results divided in two main sections:
   - Sloshing regime identification
   - Reduced Order Model identification and reliability evaluation
6. **Appendix A**: Finite volume solver used

Chapter 2

Theoretical Background

2.1 Sloshing dynamics

The present thesis tackles a cylindrical horizontal reservoir with radius $R = 1$ m, infinitely long (i.e., $L >> R$), filled halfway with liquid and subjected to a lateral excitation in the direction normal to the length.

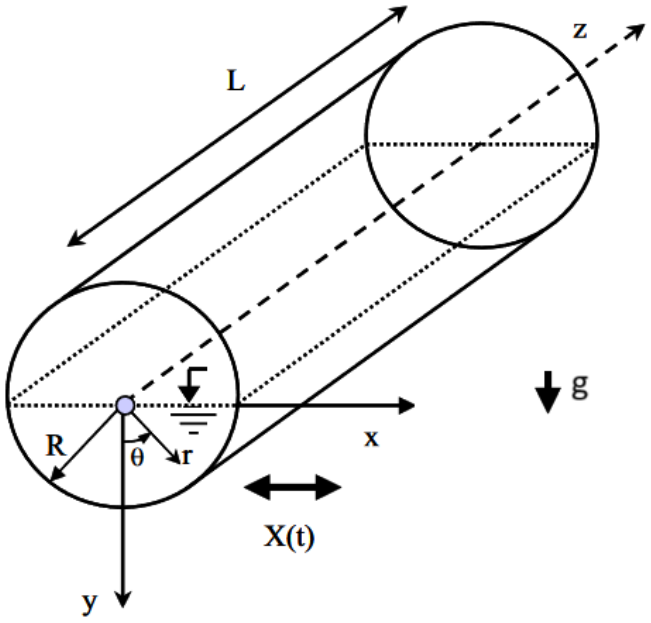

Figure 2.1: Half filled horizontal cylinder [1]

In Figure 2.1 there is represented the reference tank in cylindrical coordinates centered on the cylinder's cross-section.

The approximation of the 2-dimensional phenomenon involves some limitations. In particular, it is not possible to see how the liquid behaves in the longitudinal direction, thus not all of the physics of the phenomenon can be taken into account. Nevertheless, for reservoirs that have a fairly low diameter-to-length ratio, subjected to an excitation in the 2D plane, it can be a good approximation of the mean field of the fluid inside.

The problem of the lateral excitations applied to the tank can be presented in two ways:

1. Considering a moving reference frame, where the excitation is applied through the rigid motion of the container
2. Considering a fixed reference frame, where sloshing is introduced via changes in the acceleration applied to the fluid volume

Both approaches are analyzed in this work through Computational Fluids Dynamics simulations. By comparing them, we aim to understand whether they are equivalent or if it is preferable to choose one approach over the other.

Considering the first approach, this work imposes a harmonic displacement on the container with amplitude X_0 and frequency Ω.

$$X(t) = X_0 \cos(\Omega t) \tag{2.1}$$

With the second approach, it is imposed the x-component of the acceleration to which the fluid is subject:

$$\mathbf{f} = (-X_0 \Omega^2 \cos(\Omega t), -g, 0). \tag{2.2}$$

Equations 2.2.1 and 2.2 are the boundary conditions in the formulation of the problem.

2.1.1 Governing equations

Considering isothermal sloshing, we can assume that the liquid is incompressible, $\rho_l = \text{const}$. From this, we can assume that the velocity of the fluid satisfies:

$$\nabla \cdot \mathbf{u} = 0 \tag{2.3}$$

where $\mathbf{u} = (u_r, u_\theta, u_y)$ is the velocity of the fluid in cylindrical coordinates.

The Navier-Stokes momentum equation is

$$\frac{\partial \mathbf{u}}{\partial t} + (\mathbf{u} \cdot \nabla)\mathbf{u} = \nu \nabla^2 \mathbf{u} - \frac{1}{\rho} \nabla p + \mathbf{f} \tag{2.4}$$

where p is the fluid pressure, and ν is the kinematics viscosity, the potential formulation of the momentum equation is used to derive the relationship for the displacement of the free surface.

2.1.2 Sloshing regimes

According to Miles [9], who investigated the sloshing phenomenon for vertical cylinders, the response of the fluid can be seen in 3 regimes:

- **Planar wave regime (PW)**: With an excitation frequency away enough from the resonance frequency and with low excitation amplitude the surface liquid motion has a planar shape. It is possible to use the linear theory to describe the movement of the surface. The reduced order model that is developed in this work is identified using this regime that makes it predictable.
- **Chaotic sloshing (CH)**: Characterized by a chaotic motion and wave breaking, with many flow frequencies overlapping. Typically, the external excitation is near the resonance frequency. The wave increases the movement until the inertia equals the gravity acceleration and then there is the wave breaking.
- **Swirling sloshing (SW)**: In this regime, the waves have a rotational motion. Since this regime is by its nature 3-dimensional, in that the fluid moves in a direction transverse to the direction of excitation, the case we studied, 2D, cannot show this type of regime.

Figure 2.2 presents the sloshing regimes described above

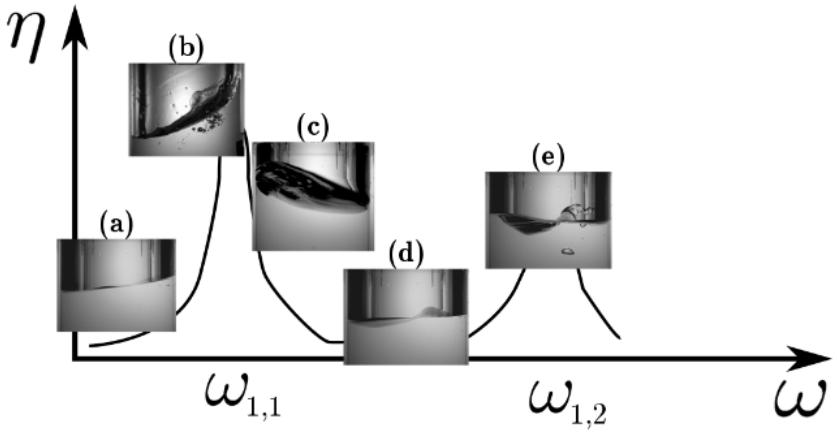

Figure 2.2: Visualisation of sloshing regimes in a vertical cylinder [2].

In figure 2.3 the phase diagram is shown applied to a vertical cylinder using Miles'[8] weakly nonlinear theory just for the first natural frequency which is the dominant one, as demonstrated in section 6.1 (and most commonly observed in practical applications [15]). the boundaries between the regimes are derived from

$$\frac{X_0}{R} = \frac{1}{1.684}\left(\frac{(\Omega/\omega_{11})^2 - 1}{\beta_i}\right)^{3/2} \tag{2.5}$$

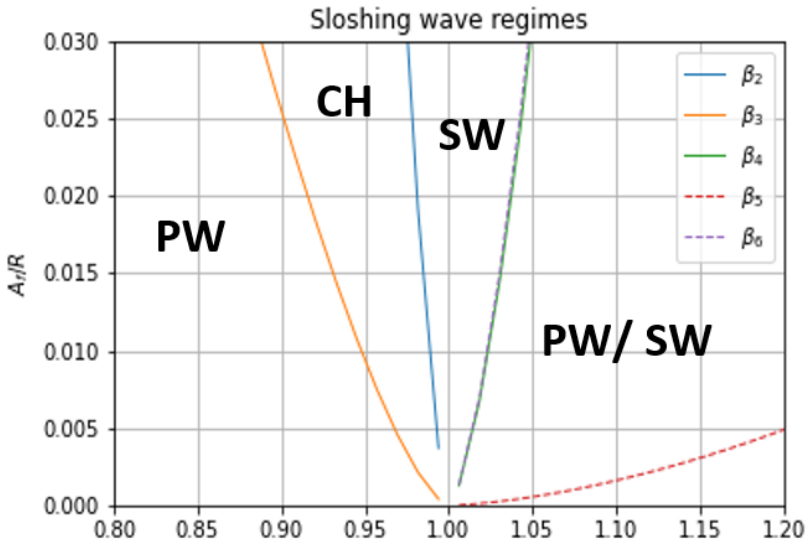

Figure 2.3: Sloshing regimes for upright cylinders

ω_{11} is the first natural frequency for an upright cylinder, β_i are fixed values that separate the different regimes: $\beta_2 = -0.36$,$\beta_3 = -1.55$,$\beta_4 = 0.735$, they are derived from stability analyses of the solution evaluated with one of the regimes.

This theory, although valid for vertical cylinders, is also valid to explain the phenomenon for horizontal cylinders although the boundary values between the various regimes are not the same.

2.2 Linear sloshing potential flow

Following the strategy described by [18][1][19] which are based on a linear model using the potential vector Φ. We reported the approximations of the linear model that uses a potential function

- Irrotational velocity field $\longrightarrow \nabla \times \mathbf{u} = 0$
- Incompressible fluid $\longrightarrow \rho = cost. \longrightarrow \nabla^2 \mathbf{u} = 0$
- $u_y(y = 0) \simeq \frac{\partial \eta}{\partial t} \simeq (\frac{\partial \phi}{\partial z})_{z=0}$
- Linear phenomena: Low velocity and small displacements
- No surface tension $\sigma = 0$
- Rigid container walls
- 2D phenomena

With this hypothesis we can build a potential function, whose directional derivative of this velocity potential function $\Phi(r, \theta, t)$, at any point in the fluid, is the velocity of the fluid in that direction at the given point:

$$\mathbf{u} = \nabla \mathbf{\Phi}$$

2.2.1 Potential solution for half filled tank

The velocity potential function $\mathbf{\Phi}(r, \theta, z, t)$ satisfy Laplace equation 2.6

$$\nabla^2 \mathbf{\Phi} = 0 \tag{2.6}$$

which in polar coordinates, using the notation described in the Figure 2.1, becomes equation 2.7

$$\nabla^2 \mathbf{\Phi} = \frac{1}{r}\frac{\partial}{\partial r}\left(r\frac{\partial \mathbf{\Phi}}{\partial r}\right) + \frac{1}{r^2}\frac{\partial^2 \mathbf{\Phi}}{\partial \theta^2} + \frac{\partial^2 \mathbf{\Phi}}{\partial z^2} = 0 \quad r < R, -\pi/2 < \theta < \pi/2, 0 < z < L \tag{2.7}$$

considering a 2D hypotesis we have also:

$$\frac{\partial^2 \mathbf{\Phi}}{\partial z^2} = 0$$

We can linearize the problem by assuming that the displacements we apply are small enough to derive the free-surface condition described by

$$\frac{\partial \mathbf{\Phi}}{\partial t} - g\eta = 0 \quad \text{at } \theta = \pm\pi/2, r < R, 0 < z < L \tag{2.8}$$

with η the displacement of the free surface, and

$$\pm\frac{1}{r}\frac{\partial \mathbf{\Phi}}{\partial \theta} + \frac{\partial \eta}{\partial t} = 0 \text{ at } \theta = \pm\pi/2, r < R, 0 < z < L \tag{2.9}$$

Another boundary condition of fundamental importance is the kinematic condition described by equation 2.10

$$\frac{\partial \mathbf{\Phi}}{\partial r} = -\dot{X}(t)\sin(\theta) \quad r = R \tag{2.10}$$

in which the forcing of our system that sets the fluid in motion appears for the first time in the set of equations. We assume a harmonic displacement reported in equation the velocity of the displacement is:

$$\dot{X} = -X_0 \Omega \sin(\Omega t) \tag{2.11}$$

Thus, we can divide the motion of the rigid body from the sloshing motion inside the tank as two contributions, the first given by the uniform motion of the outer cylinder and the second given by the motion of the fluid inside the cylinder

$$\mathbf{\Phi}(r,\theta,z,t) = \mathbf{\Phi}_U + \tilde{\mathbf{\Phi}} \tag{2.12}$$

Dividing the two contributions in this way, we have that the cylinder's motion is simply described by the equation describing its oscillation in time

$$\mathbf{\Phi}_U = \dot{X}(t) = -\dot{X}(t) r \sin(\theta) \tag{2.13}$$

and the final equation is

$$\frac{\partial^2 \tilde{\mathbf{\Phi}}}{\partial t^2} \pm \frac{g}{r}\frac{\partial \tilde{\mathbf{\Phi}}}{\partial \theta} = -\frac{\partial^2 \mathbf{\Phi}_U}{\partial t^2} \quad \theta = \pm\frac{\pi}{2} \tag{2.14}$$

From [1], we have that the solution of the sloshing motion for half-filled cylindrical tanks is given by a function of the time q multiplying a function of form which for the case of a half-filled cylinder has a very simple shape:

$$\tilde{\mathbf{\Phi}}(r,\theta,t) = \sum_{n=1}^{\infty} \dot{q_n}(t) r^n \sin(n\theta), \quad z = \text{const} \tag{2.15}$$

that can be simplified by using only the first two terms, so we can write

$$\mathbf{\Phi}(r,\theta,t) = \dot{q_1} r \sin(\theta) + \dot{q_2} r^2 \sin(2\theta). \tag{2.16}$$

Then, we derive $\dot{q_1}$ by solving the boundary condition equation 2.8 that reduces to the

$$\ddot{q_1} + 2\omega_n \zeta \dot{q_1} + \omega_n^2 q_1 = X_0 \Omega^2 \cos(\Omega t) \tag{2.17}$$

in which appears the natural frequency ω_n and the damping ratio ζ. This result comes out by considering the truncation to the first term of the proposed solution for the potential flow, where we see that the term relating to $\dot{q_2}$ for evaluating the maximum wall displacement is not needed.

Finally is it possible to derive the displacement we are interested in, η by solving the boundary equation eq. 2.8 valid for $\theta = \pm\pi/2$:

$$\eta = -\frac{1}{g}\frac{\partial \mathbf{\Phi}}{\partial t} \tag{2.18}$$

considering that we wish to extract the displacement of the surface at a fixed radius $\bar{r}$ and for $\theta = \pi/2$ which allows us to calculate the vertical displacement, the equation 2.16 becomes,

$$\mathbf{\Phi}(\bar{r}, \pi/2, t) = \dot{q_1}\bar{r}$$

therefore the displacement will be

$$\eta = -\frac{\bar{r}}{g}\ddot{q_2} \tag{2.19}$$

2.2.2 Natural frequencies and sloshing masses

Considering a non-deformable tank under transverse excitation along the x-direction is possible to derive the sloshing frequencies of the system using the procedure described in [19]. This approach identifies the sloshing frequencies as the eigenvalues of the linear system:

$$([K] - \omega_k^2[M])\Psi_k = 0, \quad k = 1, 2, 3, ..., \tilde{N} \tag{2.20}$$

in which the mass $[M]$ and stiffness $[K]$ matrices are defined as function of the particular spatial functions $[N]$:

$$[M] = \frac{1}{g}\int_\Sigma [N]^T[N]d\Sigma$$

$$[K] = \int_\Sigma [B]^T[B]dV$$

with V the volume of the fluid, and Σ the free surface area.

The indices of the mass and stiffness matrices are computed with

$$K_{mn} = \begin{cases} \dfrac{2mnLR^{m+n}\sin\left(\frac{m-n}{2}\pi\right)}{(m-n)(m+n)}, & m \neq n \\ \dfrac{m\pi}{2}LR^{2m}, & m = n \end{cases}$$

$$M_{mn} = \frac{2LR^{m+n+1}}{g(m+n+1}sin\left(\frac{m\pi}{2}\right)sin\left(\frac{n\pi}{2}\right)$$

Solving the corresponding eigenvalue problem yields the resonance frequencies for a half-filled cylinder, considering $L = 1$ m and $R = 1$ m natural frequencies ω_i of the system were obtained. It was seen how the choice of $\bar{N}$ and thus the size of the matrix system is important since the more we increase the size of the system the more the eigenvalues, natural frequencies of the system, achieve convergence. In our case $\bar{N} = 20$ was imposed to obtain the results described in table 2.1

Table 2.1: Natural frequency half filled tank

Natural frequency	[rad/s]
ω_1	3.645
ω_2	6.751
ω_3	8.754
ω_4	10.369

From this formulation, it is possible also extract the sloshing masses for the half-filled cylinder that are reported in table 2.2. It can be seen that the preponderant

mass is that relating to the first natural frequency, in according with [4], while those relating to the other resonance frequencies being orders of magnitude smaller, they can be neglected.

Table 2.2: Sloshing masses from potential theory

$m_{1\|sl}$	$m_{2\|sl}$	$m_{3\|sl}$	$m_{4\|sl}$
0.569	0.0177	0.00405	0.00153

2.3 Equivalent mechanical model

The linear models commonly used to describe the sloshing are the pendulum model and the mass-spring-damper model[20][21].

We use the latter, in this model there is a fixed mass m_0 in the bottom of the container and several mobile sloshing masses $m_{n|sl}$, these masses are connected to the container by springs and damping with stiffness k_n and damping constant ζ_n as we can see in figure 2.4

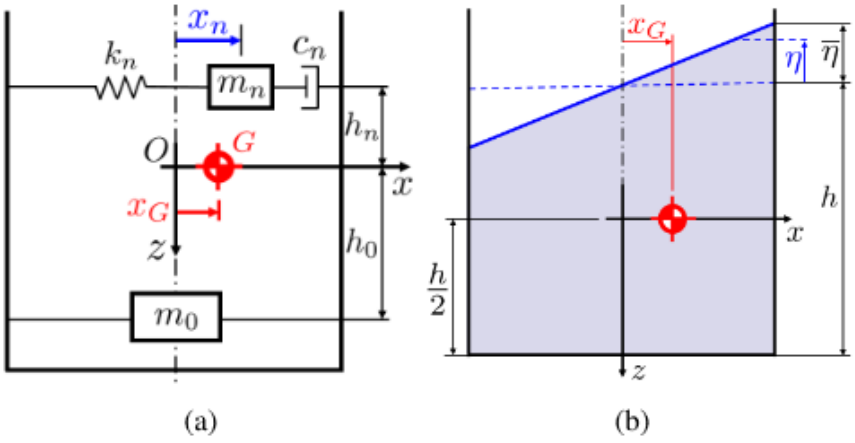

Figure 2.4: Sloshing mechanical model

According to [20], considering a container moving only along the transverse axis the motion can be described by the equation

$$\ddot{x}_n + 2\zeta_n\omega_n\dot{x}_n + \omega_n^2 x_n = X_0\Omega^2 cos(\Omega t) \tag{2.21}$$

in which x_n is the displacement of the n-th sloshing mass.

This model makes it possible to evaluate the displacement of the liquid at the wall $\bar{\eta}$, where the radius is maximum: $r = R$. However, considering that the

phenomenon considered is linear, it is possible to use interpolation to find the height of the liquid at points inside the horizontal cylinder.

The maximum height $\bar{\eta}$ is the sum of the height caused by each sloshing mass η_n

$$\bar{\eta} = \frac{4\sum_n x_n m_{n|sl}}{\pi R^3 \rho}, \tag{2.22}$$

$m_{n|sl}$, the n-th sloshing mass can be considered as a percentage of the total mass, it is possible to derive it from the potential solution as described in section 2.2.2. The total mass in our case with an half-filled horizontal cylinder is:

$$m_{tot} = \frac{\pi R^2}{2}\rho$$

The advantages of this model are:

- Obtain real-time data
- Derive responses for weakly nonlinear motion.
- It's possible to apply to any shape of tank
- It is possible to change the filling percentage of the tank and obtain result changing the natural frequency parameter ω_i

2.4 ROM formulation

The two models for extracting the surface height of the liquid inside the cylinder can now be compared:
Equation 2.21 from the mechanical model can be compared with the Eq. 2.17 from the potential model, both approaches are based on a second-order differential equation. The difference between the two models is that the mechanical model takes into account the sloshing mass and uses this information to calculate the surface height.

One of the aims of this thesis is to compare the two models, the mechanical model and the potential fluid model, to assess which model is better at identifying the reduced model, so both models were taken into account for the reduced model.

As shown in the following chapters with numerical simulations (chapter 4), the response we expect when we input a harmonic displacement/acceleration force, looking at the evolution of the height, can be divided into two, depending on the sloshing regime:

- **Planar sloshing**: In planar sloshing, looking at the evolution of the height of the surface at a fixed radius as a function of time, we monitor how the output oscillates between a maximum and a minimum value where, as time passes, the amplitude of the motion decreases. This decay occurs because, in the initial phase, in addition to the frequency of the forcer, the natural frequencies are also excited. Then, as the power of the natural frequencies is damped, periodic conditions are reached. Here, the surface height oscillates at the frequency of the forcer.

- **Chaotic sloshing**: In the chaotic regime, the behavior of the evolution of the surface with a fixed radius as a function of time is completely different, periodic conditions are never reached and the excited frequencies are many more. Moreover, in this case, where the displacements are large and therefore so are the velocities, the assumptions of the linear model decay, and the waves seen on the surface of the liquid increasingly increase in height until the force of inertia equals the force of gravity, at which time the wave falls and the cycle resumes.

Chapter 3

Nondimensionalization and Scaling

When approaching a fluid dynamics problem, scaling and non-dimensionalization are powerful techniques that allow for the simplification of the governing equations. This process also helps in identifying the key dimensionless numbers that govern the flow behavior, which can be crucial for understanding the physics involved and for scaling the results to different situations.

The advantages of presenting fluid dynamics problems in their nondimensional form are:

- Reduction in the number of parameters: By expressing the problem in terms of dimensionless numbers, making it easier to identify the controlling physical processes.
- Universal solutions: Nondimensionalization allows the results of a particular problem to be generalized and applied to other problems with similar dimensionless parameters, facilitating the comparison of different flow regimes. Very important if we are to compare the results obtained with experimental analyses.
- Enhanced insight into physical behavior: The relative magnitudes of the dimensionless numbers highlight the significance of various forces or effects, such as inertia, viscosity, pressure and gravity, in the flow field.

Dimensionless numbers can be derived using the Buckingham theorem [22] or by scaling the governing equations of the flow as described in [23], the second approach was used. In the scaling equation approach, these non-dimensional numbers are directly given by the governing equations as well as the boundary and initial conditions of the system.

3.1 Dimensionless numbers

To derive the non-dimensional numbers, we started from the momentum equation by dividing it into parameters and variables.
The reference values were chosen for the variables, and the equations were rewritten in dimensionless form by dividing by those reference quantities momentum balance for incompressible fluid.

Considering Eq. 2.4, which describes the Navier-Stokes momentum equation we change the dimensional variables with the reference quantities, chosen based on the main parameters of our phenomenon and reported in table 3.1

Table 3.1: Reference quantites for scaling

Quantity	Reference quantity
Reference length	R
Reference time	$\frac{R}{X_0\Omega}$
Reference velocity	ΩX_0
Reference acceleration	g
Reference pressure	$\rho(\Omega X_0)^2$

The non-dimensional conservation of mass and momentum equations are

$$\nabla^* \cdot \mathbf{u}^* = 0 \tag{3.1}$$

$$\frac{\partial \mathbf{u}^*}{\partial t^*} = -\nabla^* p^* + \frac{1}{\mathrm{Fr}}\mathbf{f}^* + \frac{1}{\mathrm{Re}}\nabla^{*2}\mathbf{u}^* \tag{3.2}$$

The dimensionless number that emerged is the Froude number, representing the ratio between inertia and gravitational forces, defined as:

$$\mathrm{Fr} = \frac{\text{convection}}{\text{gravity}} = \frac{\bar{V}^2}{g\bar{L}}$$

and the Reynolds number, representing the ratio between inertial forces and viscosity forces defined:

$$\mathrm{Re} = \frac{\text{convection}}{\text{viscosity}} = \frac{\bar{V}\bar{L}}{\nu} \tag{3.3}$$

where $\bar{V}$ and $\bar{L}$ are the general reference velocity and length, using the reference values defined before, Fr and Re number becomes:

$$Fr = \frac{(X_0\Omega)^2}{gR} \tag{3.4}$$

$$Re = \frac{X_0\Omega R}{\nu} \tag{3.5}$$

neglecting viscosity due to the potential solution assumption the only non-dimensional parameter is the Froude number and the non-dimensional momentum equation is reduced to:

$$\frac{\partial \mathbf{u}^*}{\partial t^*} = -\nabla^* p^* + \frac{1}{\mathrm{Fr}}\mathbf{f}^* \tag{3.6}$$

from the non-dimensioning of the kinematic boundary condition (Eq. 2.2.1) we derive two additional non-dimensional numbers that are used to define the simulation database:

$$L_1 = \frac{X_0}{R} \tag{3.7}$$

$$L_2 = \frac{\Omega}{\omega_1} \tag{3.8}$$

The first natural frequency ω_1, as reported in section 2.2.2, is a function of the tank's fill percentage and its dimensions. Since both parameters are treated as constant in this work, ω_1 is also constant. Substituting equation 3.7 into equation 3.4, we obtain the new definition for the Froude number, which becomes:

$$Fr = \frac{(L_1 L_2)^2 \omega_1^2 R}{g} \tag{3.9}$$

By defining a range of values for the dimensionless parameters L_1 and L_2, we generate the various cases to be evaluated with fluid dynamic simulations. Thus, the excitation conditions tested in work (i.e., the databse generated from CFD simulations) are reported in the simulation matrix table 3.2.

Table 3.2: Simulation matrix

Simulation parameters										
L_1	0.01	0.0325	0.055	0.0775	0.1					
L_2	0.603	0.634	0.664	0.694	0.724	0.754	0.784	0.815	0.845	0.875
	0.905	0.935	0.965	0.996	1.026	1.056	1.086	1.116	1.146	1.177

3.2 Scaling similarity

3.2.1 Geometry similarity

In order to have a scaling relationship between the simulations we have performed with experimental results, we must ensure that the ratio of the lengths of the two

set-ups are the same (e.g. the ratio of radii sholud be equal to the length ratio), possible geometry reference variables can be

- Radius of the cylinder
- Filling percentage(height of the liquid)
- Length of the cylinder

The length of the cylinder radius and thus its transverse dimensions are fixed at $R = 1$ m. The filling percentage is fixed too at 50% of the tank. The length of the cylinder is not taken into account as the model is focused on a 2-dimensional formulation of the phenomenon, both through the analytical model and the numerical simulations performed. This assumption is valid if are considered cylinders subjected to transverse forcing and sufficiently long, the theory would predict that the length tends to infinity or at least that the ratio between radius and length is sufficiently low

$$\frac{L}{R} \ll 1$$

3.2.2 Kinematic similarity

Kinematic similarity is imposed by the excitation parameters of the system derived from the boundary condition 2.10. The excitation parameters are the amplitude and frequency of the imposed harmonic displacement. These are written in dimensionless form L_1 and L_2. Besides dictating the amplitude of the motion, these parameters also dictate the observed wave regime.

These two parameters are expressed in terms of the Froude number. Thus, by preserving this parameter the kinematic similarity is confirmed

3.2.3 Dynamic Similarity

Dynamic similarity: force scale ratios are the same. It is assured if the dimensionless numbers defined in the problem are preserved.

Since the model used is that of the potential fluid, it is possible to neglect the surface tension and the viscous terms. So, the only nondimensional number is the Froude number defined with the input amplitude and frequency of the displacement applied to the tank.

By exemplifying the fluid model so much several nondimensional numbers are lost. Some are very important for sloshing such as the Reynolds number defined before and the Weber number defines the ratio between the pressure forces and Surface

tension. From the Weber number and the Froude number it can be defined the Bond number:

$$\mathrm{Bo} = \frac{\mathrm{We}}{\mathrm{Fr}}$$

With all these numbers the hydrodynamic regimes of the sloshing phenomena are defined and in figure 3.1 it is possible to see the different hydrodynamic regimes defined via the non-dimensional numbers.

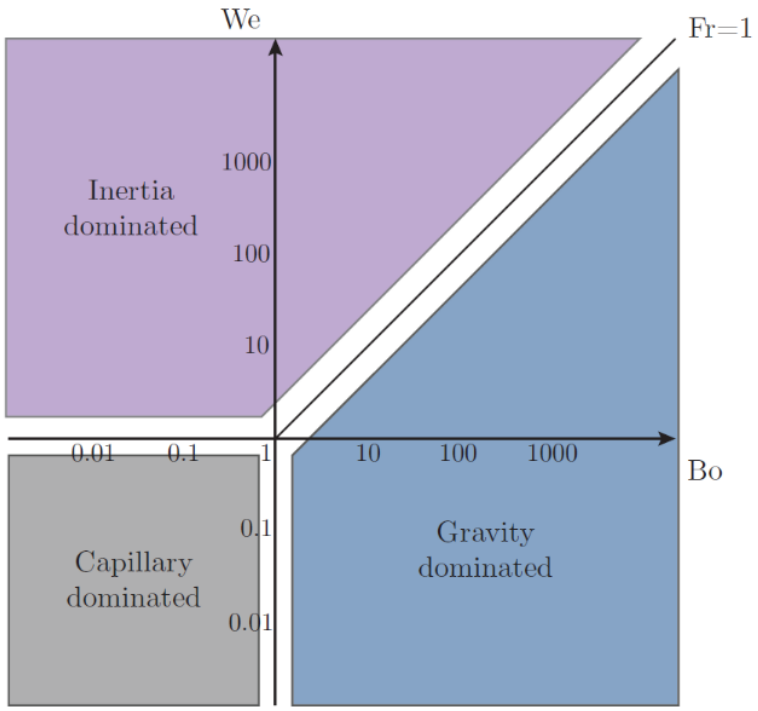

Figure 3.1: Hydrodinamic regimes [3]

An assessment of the number of Bonds makes it possible to evaluate which of the surface tension and the force of gravity has more importance in the phenomenon. Given the boundary conditions, it is to be expected that gravity will predominate and the Bond number will be very high. In any case, an evaluation of it is always appropriate to assess a priori what the sloshing conditions are.

Chapter 4

Numerical simulations for lateral sloshing

In this chapter, CFD simulations are conducted to create a database for calibrating the simplified models: the potential model and the mechanical model described in sections 2.3 and 2.2, which, given their nature of simplification, do not account for all the physics.
By simulating excitation frequencies close to the first resonance frequency, the results from potential flow or the linear mechanical model are no longer applicable. Furthermore, there is no information on the values of the damping coefficient ζ and sloshing mass $m_{i|sl}$ other than values derived from theories.

This chapter describes how the numerical simulations were set up: the software used, the convergence criteria and the methods for post-processing the results.

4.1 Numerical set-up

To conduct the simulations, the open-source software `OpenFOAM (v2206)` [24] is utilized, by using the Finite Volume Method (FVM).

After discretizing the spatial domain into an ensemble of finite volumes, the FVM implements conservation laws over the volumes comprising the mesh, transforming partial differential equations into algebraic equations. These equations are iteratively solved, adhering to boundary and initial conditions, until convergence is achieved. An overview of the cycles used is reported in Appendix A. Given the transient nature of the problem, the iteration loop is resolved for each time-step.

Parameters that change between one simulation and another are the amplitude and frequency of oscillation applied to the tank. These input parameters were chosen through changing the Froude number defined in the previous chapter.

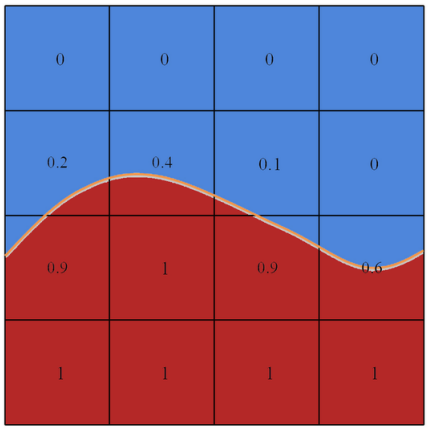

Figure 4.1: Volume of Fluids approach

The two fluids chosen for the simulations are water and air, their properties are evaluated at room temperature conditions and they are reported in table 4.1. The interface surface tension between the two phases is set to $\sigma = 0.07 kg/s^2$. Since the models used for comparison of the phenomenon are 2-dimensional, the simulations are also be 2-D.

Table 4.1: Simulation phases

Phase	Density $[kg/m^3]$	Kinematic viscosity $[m^2/s]$
water	998.2	10^{-6}
air	1	$1.48 * 10^{-5}$

4.1.1 Volume of Fluids

The solver uses the Volume of Fluids approach which is a technique used to simulate two immiscible fluids, it is used to predict the flow dynamics in free surface flows as in our case.

The VoF method [25] in OpenFOAM divides the computational domain into cells as figure 4.1 shows, and assigns each cell a fraction value that represents the volume fraction of one of the fluids. This fraction is 1 in cells fully occupied by the fluid, 0 in cells with no presence of the other fluid, and between 0 and 1 in cells that are at the interface between fluids.

In figure 4.2 we can see the α field with the half-filled tank considered in our study, in rest conditions. In the middle of the tank, we can see the interface of the surface where there is the highest gradient of α, for this reason, the refinement of the grid is applied in this region of the domain with a structured mesh. The criterion of how the mesh is refined is described later in this chapter.

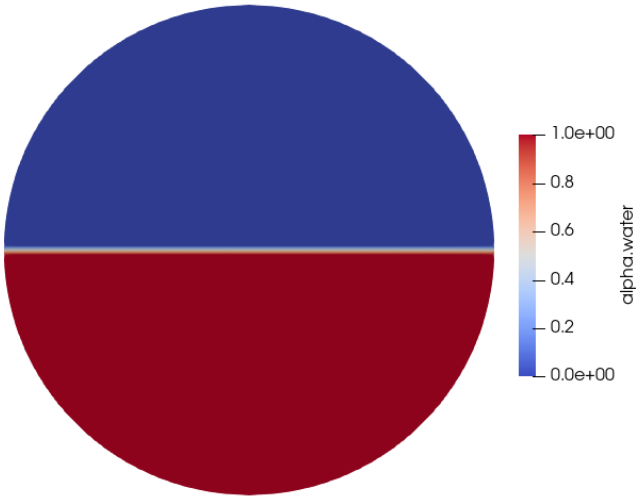

Figure 4.2: Half filled cylinder

The density ρ and the kinetics viscosity ν are defined

$$\rho = \alpha\rho_1 + (1-\alpha)\rho_2$$

$$\nu = \alpha\nu_1 + (1-\alpha)\nu_2$$

The movement of the free surface is given by solving the advection equation

$$\frac{\partial \alpha}{\partial t} + \nabla \cdot (\alpha \mathbf{u}) = 0 \tag{4.1}$$

4.1.2 interFoam solver

The solver used is `interFoam`, which allows for 2 incompressible and immiscible phases in the computational domain. It enables time-dependent simulations, allowing us to obtain the transient behavior of the simulation in isothermal conditions. The approach use the Volume of Fluids approach used in the solver is described in section 4.1.1.

The solver does not consider the energy equation as it is isothermal, the mass conservation equation consists of the incompressibility condition expressed in equation 2.3, the equation of conservation of momentum, already reported in equation 2.4, in cartesian coordinates is:

$$\frac{\partial(\rho u_i)}{\partial t} + \frac{\partial}{\partial x_j}(\rho u_j u_i) = -\frac{\partial p}{\partial x_i} + \frac{\partial}{\partial x_j}(\tau_{ij} + \tau_{t_{ij}}) + \rho \mathbf{f}_i + f_{\sigma i}$$

where τ_{ij} and $\tau_{t_{ij}}$ are the viscous and turbulent stresses and $f_{\sigma i}$ is the surface

tension. Surface tension is modeled as continuum surface force calculated

$$f_{\sigma i} = \sigma\kappa\frac{\partial\alpha}{\partial x_i}$$

whith α that is the relative percentage of one fluid in the considered cell and κ the curvature of the volume, given by:

$$\kappa = \nabla \cdot \left(\frac{\nabla\alpha}{|\alpha|}\right)$$

The pressure in this solver is:

$$p_{rgh} = p - \rho\mathbf{f}\cdot\mathbf{x} \tag{4.2}$$

where $\mathbf{x}$ is the position vector and p_{rgh} is the pressure obtained removing the hydrostatic component to the total pressure.
This change of variable modifies the momentum equation replacing the pressure with the new reference pressure.

The interface is captured by solving the advection equation with a compression term that reduces the numerical diffusion, in this compression term that is defined

$$\nabla \cdot (\alpha(1-\alpha)\mathbf{u}_c \tag{4.3}$$

where the relative velocity $\mathbf{u}_c$ is defined

$$\mathbf{u}_c = C_\alpha|\mathbf{u}|\frac{\nabla\alpha}{|\nabla\alpha|} \tag{4.4}$$

where the C_α parameter is set in the `controlDict` file and quantify the magnitude of the compression term, in the simulations that we did was set $C_\alpha = 0.1$

Table 4.2: Simulation set-up values

Variable	Value
Max Co	0.1
Max C_α	0.1
Output Sample	10 Hz
Time-tep	Adjustable
Time-scheme	Euler

In table 4.2 are reported some setup settings adopted in the simulations.

4.2 Forcing application

The sloshing of the liquid inside the tank can be implemented using two methods, as mentioned in section 2.1:

- By imposing a rigid movement of the tank, numerically, it is achieved through the motion of the mesh using the dynamicMesh tool from the software.
- Considering a reference frame that keeps the tank stationary, the acceleration term in the Navier-Stokes equations is made to be time-dependent, such that the x-component is the forcing, equation 2.2.

Both methods were tested to assess differences in the results and the simulation runtime as we describe in section 4.3.1. Following this, one was selected based on various considerations related to the results and the progression of the work.

4.2.1 Dynamic Mesh

With the dynamic mesh a rigid movement is imposed on the tank using the dynamic mesh solver adding in the `dynamicMeshDict` file, the algorithm chosen is the one below:

```
motionSolver    solidBody;

solidBodyMotionFunction  oscillatingLinearMotion;
```

in this case the mesh moves in oscillatory motion, through the amplitude and frequency inputs each point of the mesh moves according to the law

$$x(t) = X_0 \sin(\Omega t)$$

At each simulated time instant, the mesh must be regenerated, which means that we have an additional computational cost associated with this process. As described in section 4.3.1, this increase in simulation time is considerable, especially when the oscillation frequency is very close to the resonance frequency.

4.2.2 Time-dependent acceleration

After conducting tests with the dynamic mesh, we use the other approach using a time-dependent acceleration. The solver, which previously accepted a constant acceleration (typically used to represent the constant value of gravitational acceleration), has been modified to accommodate a time-dependent value, in x-Direction. The momentum equation previously reported in Eq. 4.1.2 becomes

$$\frac{\partial(\rho u_i)}{\partial t} + \frac{\partial}{\partial x_j}(\rho u_j u_i) = -\frac{\partial p}{\partial x_i} + \frac{\partial}{\partial x_j}(\tau_{ij} + \tau_{t_{ij}}) + \rho(X_0\omega^2 \cos(\omega t), g, 0) + f_{\sigma i}.$$

The modified solver, called `interDispFoam`, accepts an input file named `accelerationDict`, which contains the magnitude and frequency of the tank acceleration, as well as the gravitational acceleration in this form:

```
accelerationCoeffs
{
    amplitude (ForcingAmplitude 0 0); // [m]
    omega (ForcingFrequency 0 0);    // [rad/s]
}
gravityAcceleration
{
    gravity (0 -9.81 0);  // [m/s^2]
}
```

The implementation of this code is described in Appendix A.1.

One of the reasons for choosing this method is to utilize '`dynamicMeshRefinement`', a technique for adapting mesh refinement based on the gradient of one variable, in this case, α. This approach allows to refine the mesh in proximity of the surface interface, where there's a need for higher resolution to accurately evaluate the interface position, while creating a coarser mesh in areas of lesser interest.
This strategy aims to reduce the number of cells and, consequently, shorten simulation times by concentrating computational resources on the most critical areas.

However, the `dynamicMeshRefinement` was later abandoned due to conflicts between the dynamic Mesh Refinement tool, which works well for 3-D domains or 2-D structured mesh, but creates problems for our conditions, polar mesh, and 2D domain.

These two approaches are compared in section 4.3.1, the outcomes of that comparison determine the strategy employed to generate the database.

4.3 Simulation outputs

The quantities of interest taken from the simulation for the sake of comparison with reduced-order models are:

- The height of the free surface for a specific point at a fixed radius as a function of time. The point chosen is for $\bar{r} = 0.75$ m as can be seen in figure 4.3.
- The pressure distribution at the wall of the domain.

to obtain a visual result of the simulations, the entire field of results was also saved for certain simulated instants.

For the height extrapolation, a certain number of probes are inserted along the line shown in figure 4.3, which outputs the value of α at the fixed sampling frequency of 10 Hz.
These values are interpolated to determine the height of the interface location which we approximate to the height relative to $\alpha = 0.5$. With good approximation, this point can be considered as the location of the liquid's free surface.

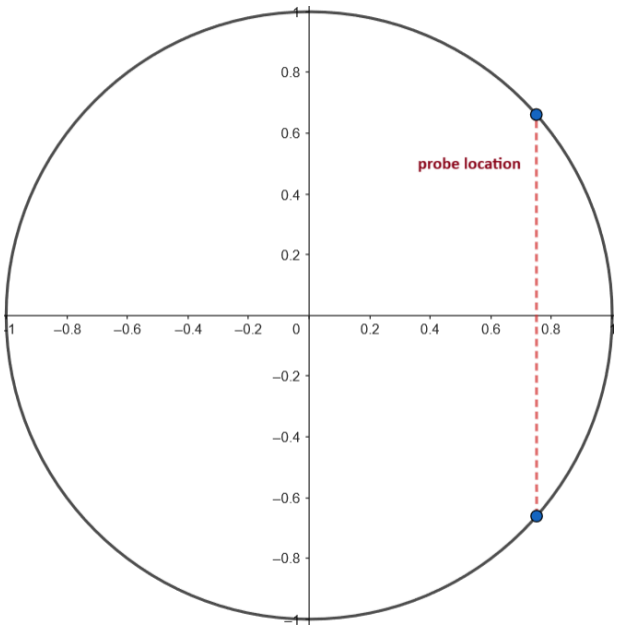

Figure 4.3: Probe location

The second parameter is the wall pressure distribution, where a series of probes provide pressure information normal to the domain with a specific acquisition frequency of 10 Hz. By decomposing the pressure into the two Cartesian contributions x and y, and integrating these components along the reference surface (which, in this case, is the arc of a circle between two continuous probes), the force in the two Cartesian directions can also be determined.

As shown in figure 4.4, the pressure contribution in the transverse direction to the tank is depicted for a specific simulation time. Observing the contribution on the y-axis reveals it to be orders of magnitude greater than the contribution in the x-direction. This discrepancy is attributed to the weight force of the fluid, which, in the scenario under consideration, is primarily exerted in the y-direction.

From the wall pressure probes, the position of the center of gravity can also be

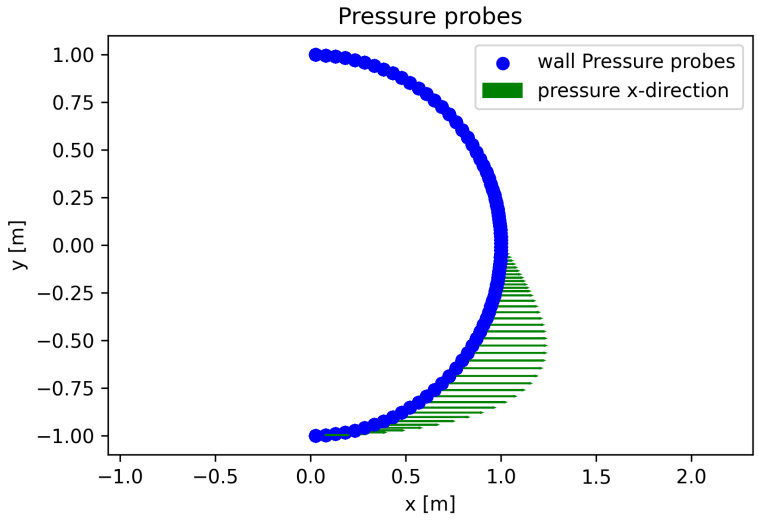

Figure 4.4: Pressure x-direction

derived by calculating the the torque, per unit length, in the two directions:

$$T_x = \sum_i x_i \cdot p_i \tag{4.5}$$

$$T_y = \sum_i y_i \cdot p_i \tag{4.6}$$

where T_x and T_y are the torque per unit length relative at each probe, then dividing by the sum of the pressures, the coordinates of the center of gravity are obtained

$$x_{CG} = \frac{T_x}{\sum_i p_i} \tag{4.7}$$

$$y_{CG} = \frac{T_y}{\sum_i p_i} \tag{4.8}$$

In rest conditions, the center of gravity of the tank with respect to the center of the cylinder is:

$$x_{CG} = 0.0008 \text{ m}$$
$$y_{CG} = -0.733 \text{ m}$$

and is also shown in figure 4.5, the motivations about the x-position of the CG that is not exactly centered in 0 should be a caused by the mesh or by the finite number of pressure probes..

4.3.1 Simulation strategy comparison

It is crucial to verify whether the two approaches, dynamic mesh, and time-dependent acceleration, yield the same results and thus prove to be equivalent.

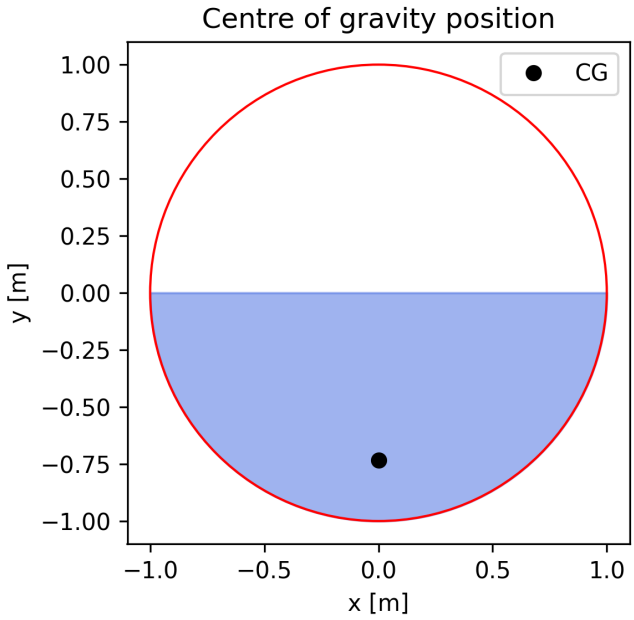

Figure 4.5: Centre of Gravity in rest conditions

For these reasons, the relevant data have been extrapolated, and figure 4.6 shows the difference between the two approaches. In this case, simulation No. 42 ($L_1 = 0.0325$, $L_2 = 0.633$) was taken as a reference, comparing the two simulation methods at the initial and final moments.

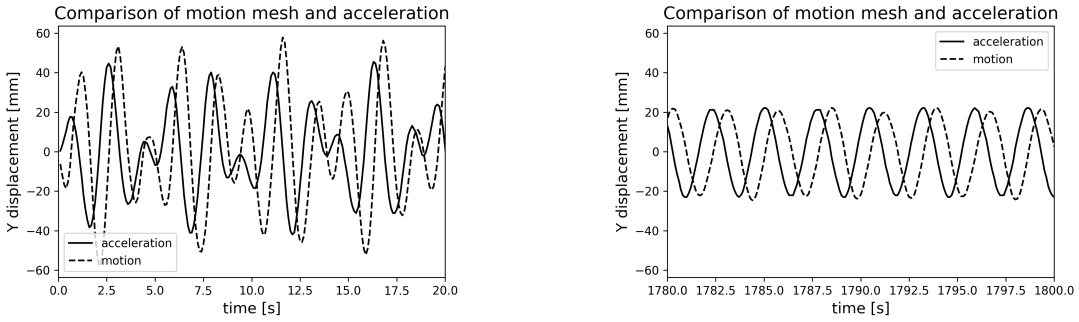

Figure 4.6: Dynamic mesh vs. acceleration

It can be observed that, initially, the simulations are not in phase. This discrepancy arises from the method of acceleration implementation within the solver; specifically, the time-dependent acceleration utilizes a cosine function, whereas the dynamic mesh employs a sine function. Despite this phase variation, it is evident that the solution involving the moving mesh exhibits higher surface height values than the acceleration.

Especially in the transient, we can better see the difference between the two approaches by plotting the envelopes, a technique to track the peaks of the simulation better described in section 5.1, of the two simulations in figure 4.7. Although

under periodic conditions the maximum height reached is the same for the two simulations we have a not inconsiderable difference between the two approaches in the transient. Surface height at initial instants is 22% greater for dynamic mesh than the time-dependent acceleration.

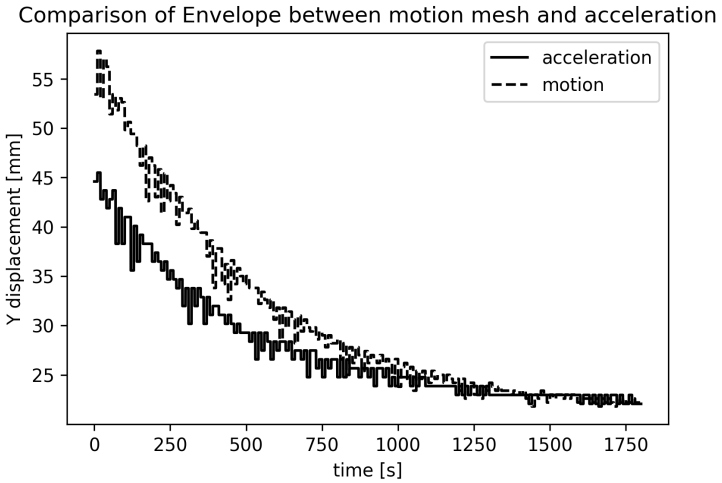

Figure 4.7: Dynamic mesh vs. acceleration: Envelope

Another problem identified with using the dynamic mesh is that, at each time step, the solver has to reconstruct the computational grid, which increases the simulation runtime.

To show this, a benchmark was conducted. test by considering 2 simulations, one near resonance and the other far from resonance as an example of planar and chaotic regime (Sim No. 42 $L_1 = 0.0325$, $L_2 = 0.633$, Sim No.54 $L_1 = 0.0325$, $L_2 = 0.996$). As observed in the figure 4.8, we show, for each second of physical simulation, how many seconds of computational simulation are used.
These benchmark tests were carried out using the same hardware under the same operating conditions.

Considering the necessity to conduct numerous simulations, it is preferable to minimize simulation time.

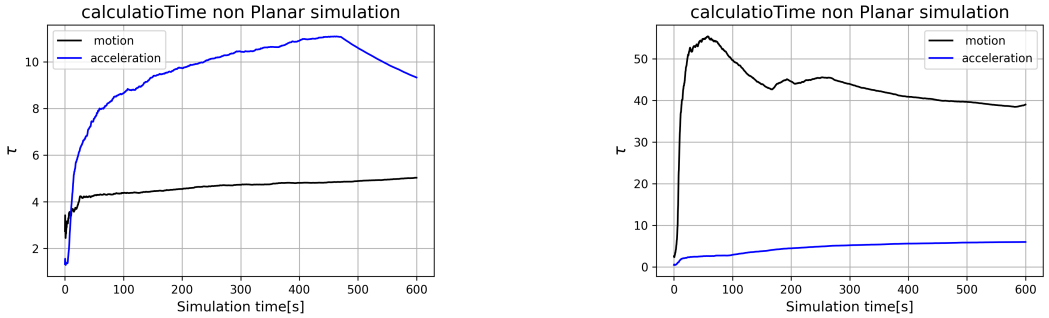

Figure 4.8: Calculation Time

Defining τ a parameter representing the time it takes the software to simulate one second of physical time If an average of the simulation times is considered with the two approaches, simulations using a dynamic mesh realize a +820% of average simulation time for the chaotic simulation and +51% for the planar simulation.

From the tests and considerations reported in this section, it was decided to choose the time-dependent acceleration for the simulation strategy. In this way, we greatly reduced simulation times, especially under chaotic conditions. A comparison study with experimental data is deemed necessary.

4.4 Grid convergence study

A grid study is conducted to evaluate the required level of grid refinement necessary to achieve consistent results. Especially for sloshing simulations the choice of the mesh plays a critical role in the success of the simulation. The effects of the wall are by no means negligible, a large part of the sloshing mass is in contact with the wall where friction develops and tends to dampen the movement.

Given the geometry of the domain, represented by a 2-D circle, a semi-polar mesh is utilized, wherein a band is defined of varying height in the center in which a structured mesh is to be constructed. This hybrid approach is used because building a structured mesh over the entire domain is complex due to the presence of wall curvature, whereas a purely polar mesh would have problems in the center of the domain where the polar lines converge, resulting in cells with too much difference in size.

The criterion for choosing how refined the mesh starts from the results of the potential flow theory, at least in cases where it fell within the planar sloshing regime. The AR ratio parameter was defined. between the cell's height in the refinement zone and the wave's height according to the potential theory, section 2.2:

$$AR = \frac{\text{Cell Height}}{\text{Potential Height}}$$

Then, a series of simulations was conducted wherein this ratio was gradually decreased until a plateau value was reached through calculation.

Once these convergence conditions were reached, the ratio was maintained constant and applied in all simulations to derive the height of the cell in the refinement zone. Therefore, with this approach, a different mesh is employed for each simulation (since the periodic-state maximum height varies for each forcing). Just one simulation with specific amplitude and frequency values, away from resonance, was used to assess this ratio.

Since most of the fluid is in contact with the wall, the addition of a structured boundary layer is fundamental in our mesh. As described in [26], excluding a

Boundary Layer near the wall yields significant differences in the final results, viscous damping effect captured by the boundary layer grid also has an important influence on wave elevation.

According to this reference, the boundary layer thickness can be estimated as

$$y_{BL} = \frac{4.6}{\sqrt{\omega_1/(2\nu)}}.$$

Since the resonance frequency depends only on the percentage of cylinder fill and on the Radius of the cylinder, we have a constant value of Boundary Layer refinement height, $y_{BL} = \text{const.}$.

As depicted in Figure 4.9, including wall-structured mesh results in increased damping throughout the cylinder. Notably, both the periodic wave height and damping factor exhibit variations. With the additional damping introduced by the boundary layer, it is observed that the wave height diminishes, while the transient behavior is characterized by more pronounced damping.

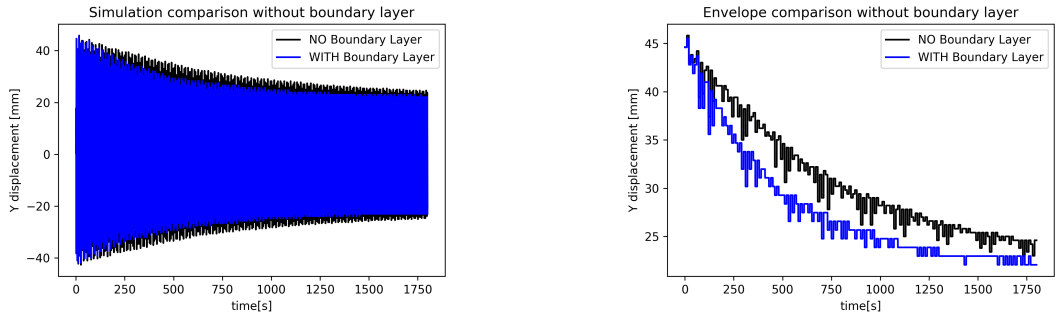

Figure 4.9: Simulation comparison without Boundary Layer

For grid studies, the simulation began with the coarser grid and was gradually refined to lower the aforementioned ratio.

Once the fluid motion becomes purely harmonic for one mesh, the result of that mesh is interpolated onto a finer mesh using the OpenFOAM tool `mapFields`. It's a utility for transferring field data (i.e. pressure, velocity, and α in our case) between different meshes and is useful for comparing results across refining meshes.

Subsequently, the simulation is restarted to reach the periodic state again for the new mesh, and the differences between the meshes are evaluated until convergence on the periodic height from one mesh to another is achieved.

In particular, this work was carried out for a case where it was known that the phenomenon resulted in pure planar motion, namely for $L_1 = 0.01$ and $L_2 = 0.68$. In table 4.4 we reported the values for the meshes, and in figure 4.14 are shown the values of height of the free surface at $r = 0.75$ m. The periodic peak height is

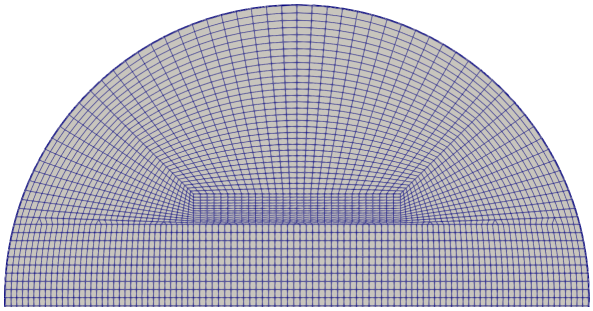

Figure 4.10: very Coarse mesh

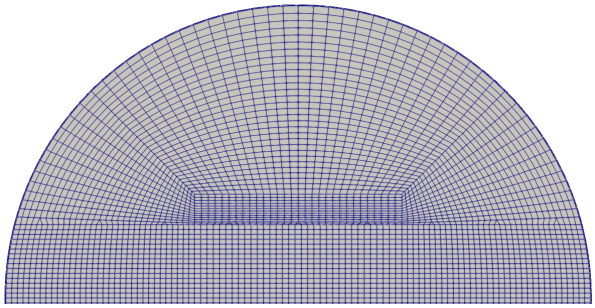

Figure 4.11: Middle mesh

taken by taking an average of the height in the last 3 peaks in steady conditions. In figure 4.10,4.11 and 4.12 we reported 3 meshes from the grid refinement study

After this study, free-damping simulations were conducted: once convergence in the meshes had been reached, the acceleration in the x-direction was set to 0 letting the system dampen the oscillatory movement.

Figure 4.13 shows that in this case, the choice of mesh plays a significant role, much more so than in simulations where acceleration was present. In this case, the damping factor varies considerably from one mesh to another and then settles at a constant value.

Once the free damping envelopes are obtained, the damping coefficient is evaluated

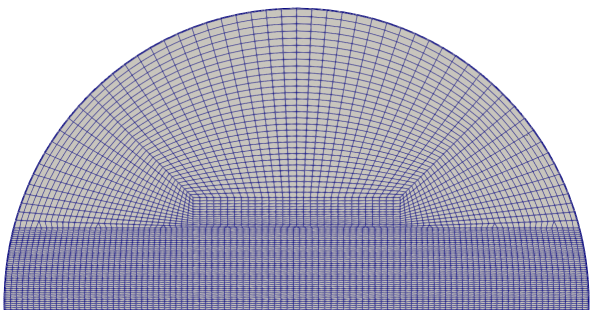

Figure 4.12: Fine mesh

ζ by using the average logarithmic decrease[27]:

$$\bar{\delta} = \sum_n ln\left(\frac{\eta_n}{\eta_{n+1}}\right)$$

$$\zeta = \frac{\bar{\delta}}{\sqrt{4\pi^2 + \bar{\delta}^2}}$$

in table 4.3 the evaluation of ζ is reported for the meshes used.

Table 4.3: Damping coefficient in free damping

Mesh	ζ
very Coarse	0.007848
Middle	0.005451
Fine	0.005431
very Fine	0.005429

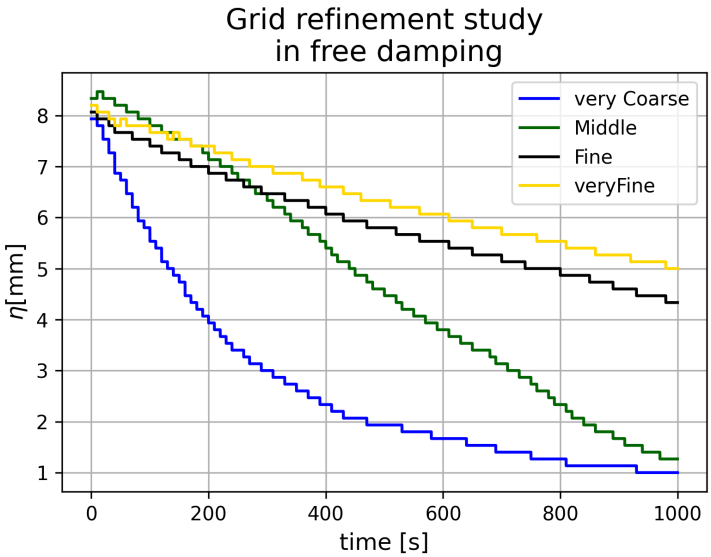

Figure 4.13: Grid refinement study in free damping

Table 4.4: Grid studies

Mesh	**Layers number**	**Cell height [mm]**	**CFD periodic height [mm]**	**AR**	**CFD/potential [-]**
Very coarse	20	20	9.216	2.068	0.953
Coarse	34	11.765	8.810	1.217	0.911
Middle	46	8.696	8.603	0.899	0.890
Fine	66	6.061	8.683	0.627	0.898
Very fine	80	5	8.750	0.517	0.905

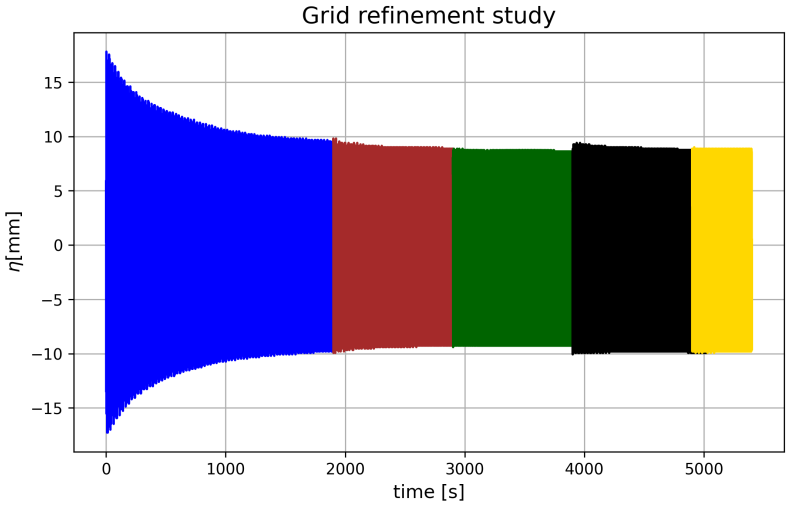

Figure 4.14: Grids refinement

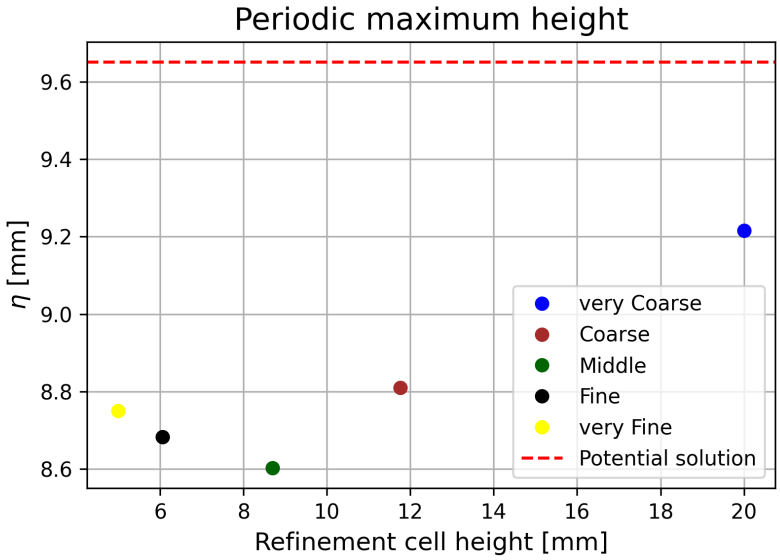

Figure 4.15: Grids refinement study

After these considerations, the process involved selecting the most appropriate AR value, considering both the convergence of the peak value of the wave height and the free damping factor. This led us to choose, as shown in the table4.4

$$AR = 0.627$$

By simulating in free damping, however, it was seen that the value of AR varies considerably between the "Middle" and "Fine" meshes, while it differs little between the latter two meshes. This led us to choose the "Fine" mesh for the correct value of AR.

Chapter 5

Reduced-order model calibration

Various optimization algorithms were used to identify the reduced model, based on minimizing a variable that indicates how far the model deviates from the results produced by CFD.

In this part of the thesis we aim to employ the results derived from CFD to formulate an optimization problem from which we can fit the results of the mechanical model, thereby identifying its unknown parameters. From this model, the two unknowns are the damping coefficient and the percentage of mass relative to the first sloshing mode. These two parameters must be optimized to match the envelope of heights from the CFD simulations with those predicted by the reduced model.

5.1 Cost Function

The cost function, quantifies the difference between the predicted output of the model and the actual output, which in our case are the CFD results. It serves as a measure of error or loss, guiding the optimization process.
The goal of the optimization part is to minimize this value to find the optimal parameters of the model. The choice of cost function depends on the nature of the problem and significantly influences the effectiveness and convergence of the optimization algorithm used.

Three types of cost functions were tested, based on the mean square of some function of the difference between the predicted function and the CFD data, this 3 difference functions are:

1. Difference **Point to point**
2. Difference between **Hilbert transforms** functions

3. Difference between **Envelopes**

Point to point difference: we subtract the height of the surface extracted by the CFD from the height of the surface output of the reduced model time instant by time instant. The cost function is defined

$$J = \sum_i (\eta_{model,i} - \eta_{CFD,i})^2$$

main problem using this approach is that if the predicted data from the model is not in phase with the CFD data the does not provide valuable insight on the model performance.The main reason it does not work is because if the reduced model result gives us a solution that is not exactly in phase with the numerical results, the cost function is comparing different time instants. And so you are not comparing the model with the numerical results in the best possible way.

Hilbert transform: Hilbert transformation is a mathematical operation that transforms a real-valued function into another real-valued function, providing the analytic signal from the original function. The transform is found by calculating the convolution of the signal $x(t)$ with the function $h(t) = 1/(\pi t)$.
The equation to find this transformation is defined as follow:

$$H(x)(t) = \frac{2}{\pi} \lim_{\varepsilon \to 0} \int_{\varepsilon}^{\infty} \frac{x(t-\tau) - x(t+\tau)}{2\tau} d\tau$$

The Hilbert transform of a signal is a useful tool because it gives us the envelope of the peaks of our function. Having this envelope shape, the cost function is constructed. as the difference between the Hilbert transform predicted by the model minus the CFD transform:

$$J = (H(\eta_{model}) - H(\eta_{CFD}))^2$$

One problem encountered in this formulation is the strong presence of secondary peaks in the signal, both from the model and from CFD. This gives us a Hilbert transform signal with a strong oscillation, which we tried to correct with a low-pass filter.

Envelopes: finally, the decision was made to utilize the envelope of the signal constructed skipping the peaks within a period of our choice. To evaluate the envelope we divide the signal into a discrete number of time steps, for each time step we calculate the maximum height of the liquid in that interval, the envelope of the signal will be the conjunction of the envelopes of each interval.

This last way of defining the cost function is the one that has proved to be the best for evaluating the difference between the predicted values and the CFD data.

$$J = (Env(\eta_{model}) - Env(\eta_{CFD}))^2$$

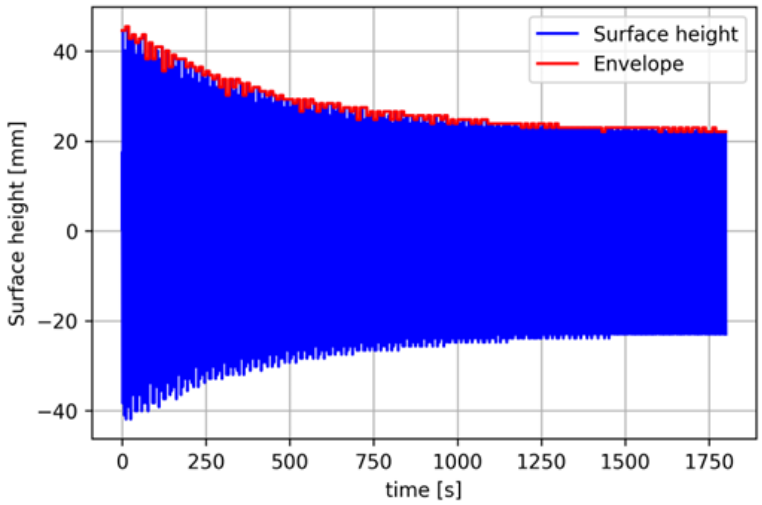

Figure 5.1: Peaks envelope

Figure 5.1 shows the envelope algorithm applied in one simulation.

In the point-to-point solution and the unfiltered Hilbert transform the optimizer can't find better values of parameters than the first guesses. The filtered Hilbert function and envelope provide better converge behavior. The main reason for this is that with the first two cost functions, multiple minima were found, which if evaluated would show up as non-optimal. Whereas for the envelope after the optimiser has reached the minimum result, we see how the solution, if we consider a single simulation, matches the reduced model with the CFD results.

Therefore, the envelope was chosen as the cost function.

5.2 Optimization algorithms

Three optimization algorithms were used:

- **BFGS**: developed by Broyden, Fletcher, Goldfarb, and Shanno employs the quasi-Newton approach[28]. This technique relies solely on first derivatives and has demonstrated effective results in optimizing even non-smooth functions.
- **Nelder-Mead**: employs the Simplex algorithm[29]. This approach is dependable across a wide range of applications. Nonetheless, in cases where the numerical calculation of derivatives is reliable, algorithms that utilize first and/or second-derivative information may generally be favored due to faster convergence.
- **Stochastic Gradient Descent**: Unlike traditional gradient descent, which

calculates the gradient of the loss function using the entire dataset to update model parameters, SGD updates parameters using only a small batch of samples at a time. This approach makes SGD much faster, allowing for efficient training of models on large datasets. The stochastic nature of the algorithm, which introduces randomness in the selection of data points, helps in avoiding local minima and can lead to better generalization on unseen data.

5.3 Optimization with multiple simulations

It was decided to start the optimization process by considering only one simulation, thus finding the desired parameter values. Then these parameters were used as initial guesses into the optimization that considers all the planar cases.

To do this, we consider all simulations in the cost function that is defined:

$$J = \frac{1}{J} \sum_{j}^{J} \left(Env(\eta_{model,j}) - Env(\eta_{CFD,i}) \right)^2$$

where index J is the number of simulation considered. In this way, we take an average of the cost functions of each simulation.

Chapter 6

Results

The results reported in this chapter are divided into two sections the first in which we characterize the sloshing dynamics, verifying the sloshing regime for each simulation, and the second deals with ROM identification from numerical data.

A summary of all simulated cases is shown in the figure 6.1 where the Froude number is plotted as a function of L_2, each point on the graph is a different forcing condition so a different simulation. Froude number that has as input both L_1 and L_2 defines completely the input of the simulation.

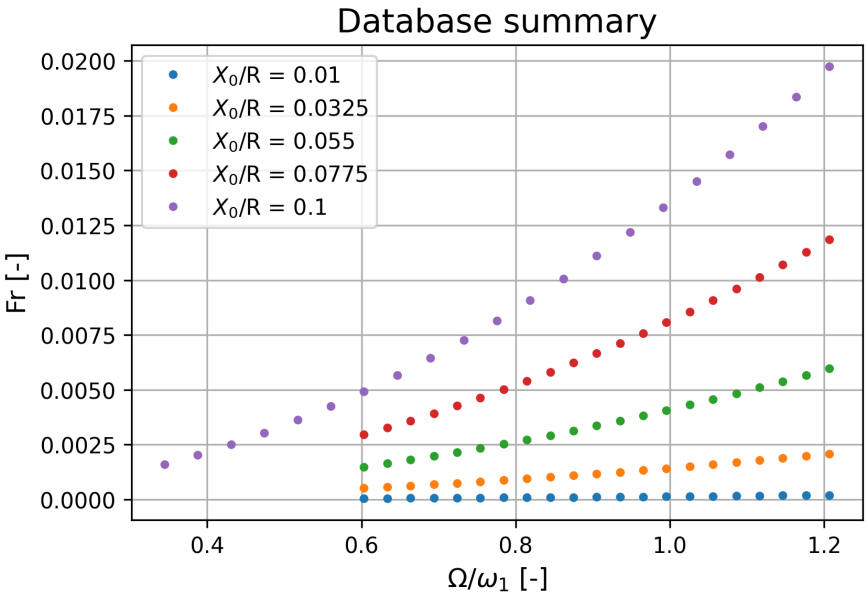

Figure 6.1: Simulation matrix

6.1 Sloshing regime identification

As mentioned in the first chapter 1, sloshing depends on the amplitude and frequency of the forcing, and can occur in two regimes: the planar regime and the chaotic regime. The ROM, built on a linear model, can only predict those simulations that fall into the former category. To assess the type of regime, the evolution of height as a function of time was viewed and the phase plane plots described below were exported.

In this section, two simulations are shown, one falling in the planar regime (sim ID. 42: $L_1 = 0.0325$, $L_2 = 0.63$) and one in the chaotic regime (Sim ID. 53: $L_1 = 0.0325$, $, 0.96$), to show the differences between the two conditions and to establish the criterion to identifying the sloshing regime.

In figure 6.2 (a) the surface of the liquid at two successive time instants is shown, as can be seen for the planar solution the displacement of the points is relatively little. On the other hand, figure 6.2 (b) is an example of a chaotic regime, it is possible to see that especially near the wall where there is a large mass displacement and a large velocity of displacement of the surface, as well are present wave jump. This underscores the impracticality of employing linear approximations in scenarios where the phenomenon lacks a planar nature.

6.1.1 Wave height at fixed point

In Figure 6.3 and 6.4 the liquid height is plotted as a function of time for the two cases mentioned before and, through the Fourier transform, the frequencies excited during both the transient and steady state.

From the height graphs, we observe two completely different behaviors for the two forcing conditions. The first in the planar regime has a transient that is extinguished after a certain period, while the second in the chaotic regime has no harmonic character anywhere in the simulation. As illustrated by the latter plot there is no symmetry around the initial position if the regime is chaotic, this is a problem in the realization of the reduced model because the models are derived from second-order dynamical systems that have solutions that do not admit this behavior.

From the Discrete Fourier transforms of the surface height signal as a function of time, figures 6.3 and 6.4, it is possible to see both the frequency of the imposed displacement with its harmonics, which have a non-negligible amplitude and the natural frequencies, especially the latter has a large amplitude that manifests itself in the transient. Furthermore, for the chaotic simulation, we see how the amplitudes of the transform are very high at all frequencies, compared to the planar transform, this is due to the chaotic nature of the regime we are in where the

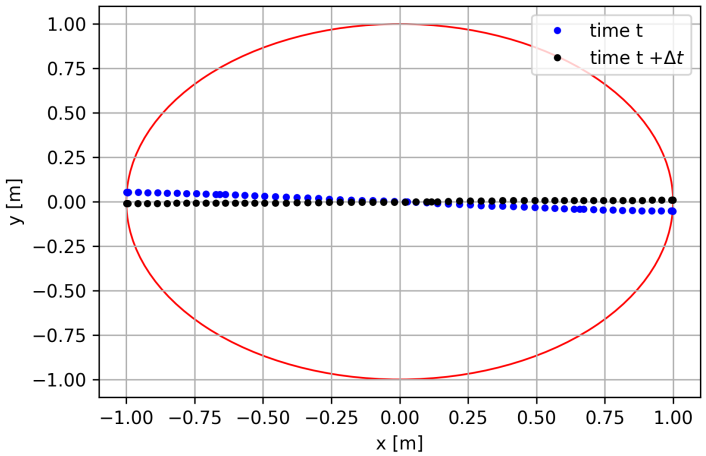

(a) Planar regime

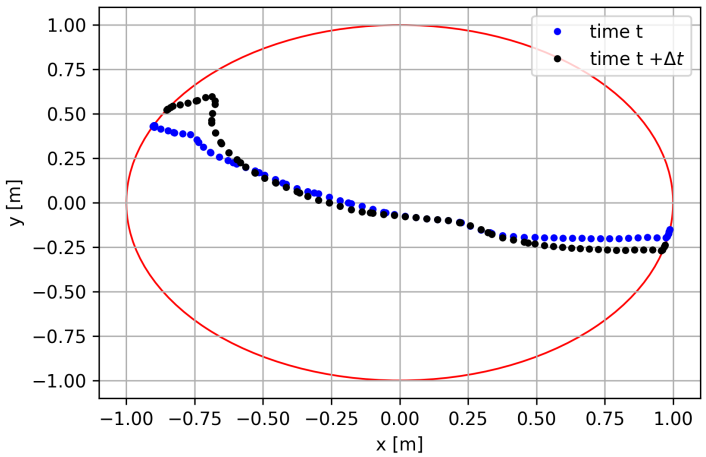

(b) Chaotic regime

Figure 6.2: Free surface position

highest frequencies are the excitation frequency but the others are not negligible.

Another tool that gives us information beyond the discrete Fourier transform is the Short-Time Fourier Transform, this gives us information about the power of a relative frequency as a function of time. Refer to Figure 6.5 (a) for an illustration of the planar regime. This figure highlights the frequency of the forcer, constantly active throughout the simulation, visible at the bottom. The strip at the top represents the resonant frequency. Initially, this resonant frequency showcases a higher power. It then gradually decreases as the fluid starts to oscillate solely at the force's frequency.

Figure 6.5 (b) presents a different scenario, depicting a chaotic case. Here, the frequency closely matches the resonant frequency. The graph's bottom band illus-

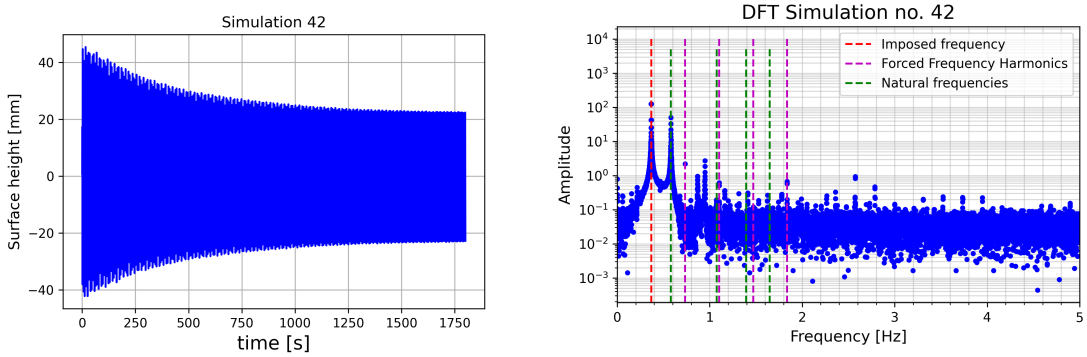

(a) Fluid height Sim no. 42 (b) Fourier transform Sim no. 42

Figure 6.3: Surface height planar simulation

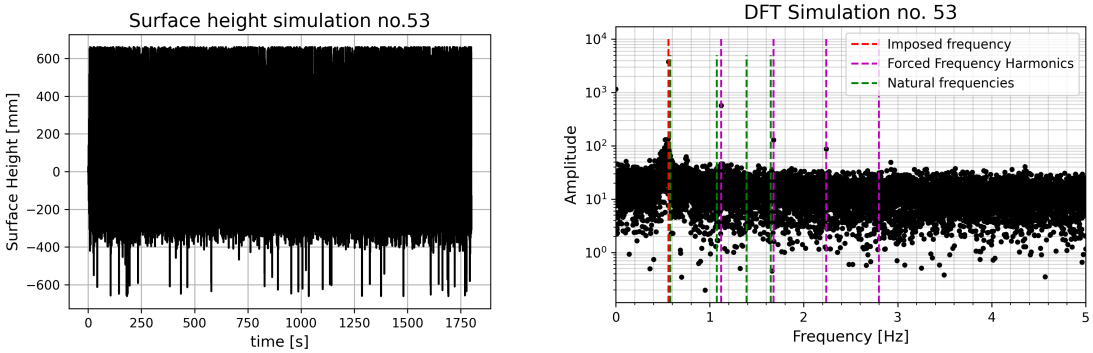

(a) Fluid height Sim no. 53 (b) Fourier transform Sim no. 53

Figure 6.4: Surface height chaotic simulation

trates the forcer's frequency, which is almost indistinguishable from the resonant frequency due to the graph's resolution limitations. The top band introduces the second resonant frequency, absent in the first graph. Though subtle, this second resonant frequency slightly contributes to the system's response frequency.

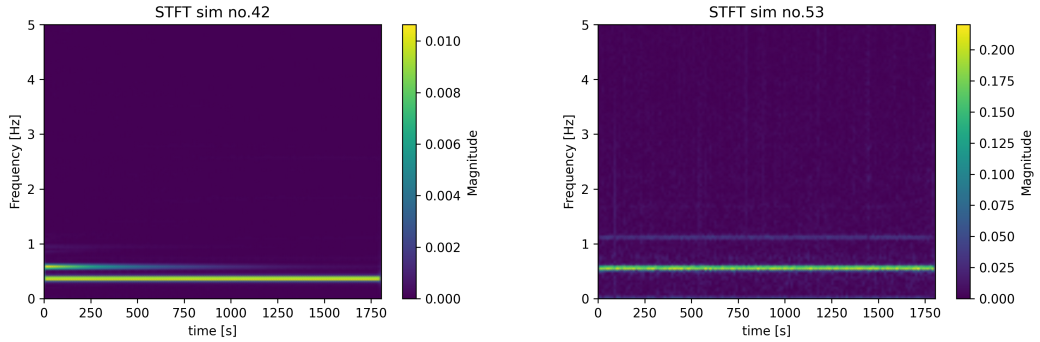

(a) Planar simulation (b) Chaotic simulation

Figure 6.5: STFT applied to the surface height time-series.

6.1.2 Centre of gravity

From the measurements made with the pressure probes on the wall, the position of the cylinder's center of gravity is derived as a function of time to observe how the position of the center of gravity fluctuates and determine if there is a law governing its movement.

To show these results, the same simulations of the previous section are chosen: in figure 6.6 we plot the x-displacement of the center of gravity with its associated Fourier transform, while figure 6.7 shows the y-displacement for simulation no. 42, figure 6.10 and 6.11 with the results for simulation no. 53.

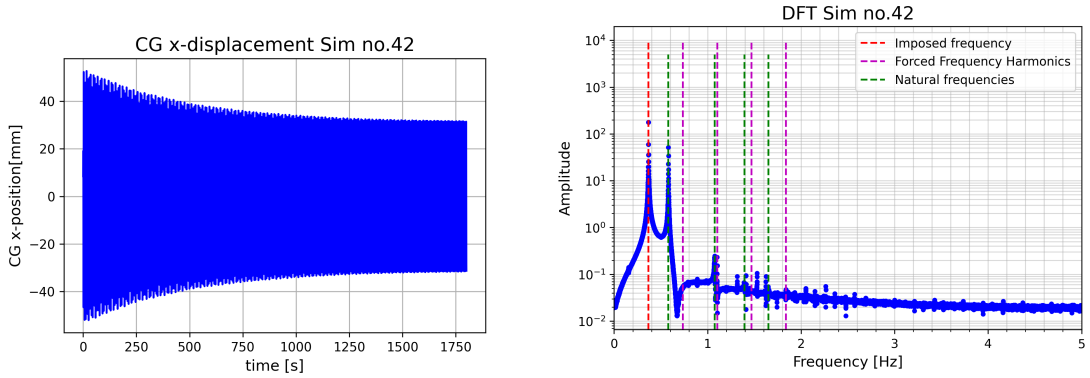

(a) Displacement of CG sim no.42 x-direction

(b) Fourier transofrm x-CG-displacement sim no. 42

Figure 6.6: Centre of gravity displacement x-direction planar simulation

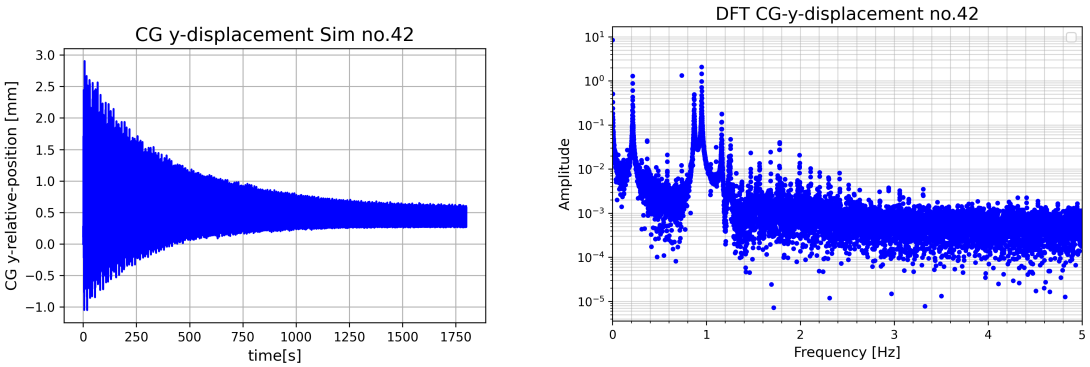

(a) Displacement of CG sim no.42 y-direction

(b) Fourier transofrm y-CG-displacement sim no. 42

Figure 6.7: Centre of gravity displacement y-direction planar simulation

The displacement in x for the planar simulation follows a very similar law to that described for the displacement of the fixed radius surface, and the DFT also confirms that the frequencies involved are that of the forcing and the first resonance frequency. Furthermore, comparing the DFT of this signal with that of

the surface position shows that it is cleaner with far fewer and more pronounced peaks. On the other hand, the x-position of the CG for the non-planar simulation has a different behavior, but this time, unlike the surface, the signal is symmetrical over the initial position, which would more easily allow the creation of a differential model that fits both the planar and non-planar cases.

Referring to the y-position of the centre of gravity, for the planar example figure 6.6 and 6.7 there is an oscillation that will cause the CG position in the y-direction to oscillate around a point when the transient is over, for the non-planar simulation, figure6.10 and 6.11, the behaviour is different and there are many more peaks which cause the centre of gravity to drop, these are due to the sloshing wave that detaches itself from the surface and falling back very abruptly lowers the centre of gravity, this phenomenon can be seen from the α field of the CFD simulations and therefore it is possible to extract the frequency at which the waves detach and fall back. The last affirmation is possible to see in figures 6.8 and 6.9 were where the α field for two successive instants is shown with the position of the centre of gravity as a function of time alongside. It can be seen how passing from t to $t+\Delta t$ there is an abrupt collapse of the position of the barycentre with respect to the y-axis to which corresponds the collapse of the wave.

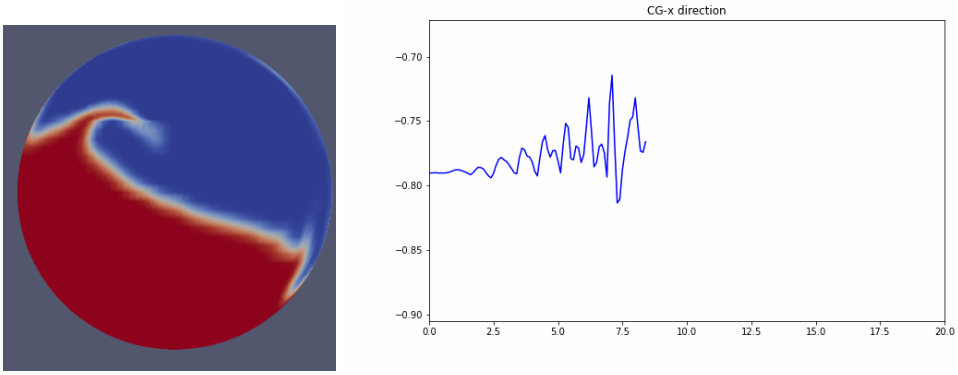

Figure 6.8: Wave breaking $t = \bar{t}$

With regard to the frequency, figure 6.7(b) and 6.11(b), analysis in the figures, it can be seen that the frequencies with more power for the y-direction of the centre of gravity are neither the frequency imposed by the forcer nor the natural frequency of the cylinder.

Figure 6.12 shows a zoom of the figure 6.11 for the first 30 seconds simulated. It can be clearly seen that even if the total regime is not planar, it is possible to derive a law, at least for the position in x of the barycentre that approximates its time evolution.

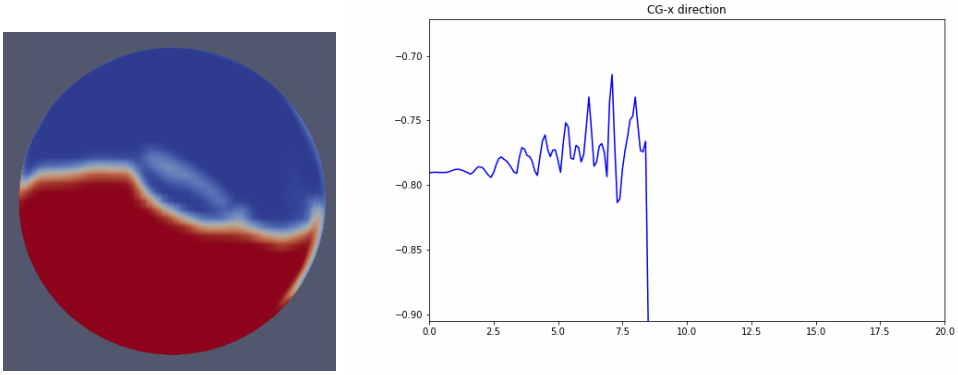

Figure 6.9: Wave breaking $t = \bar{t} + \Delta t$

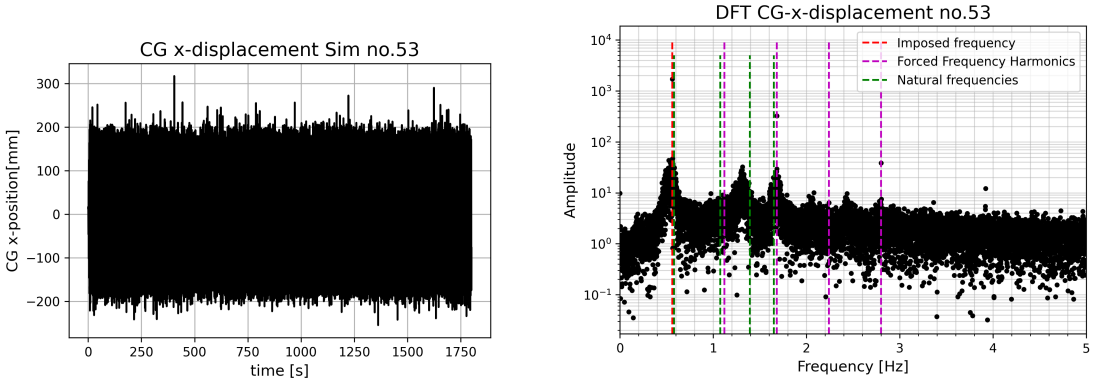

(a) Displacement of CG sim no.53 x-direction

(b) Fourier transform x-CG-displacement sim no. 53

Figure 6.10: Centre of gravity displacement x-direction chaotic simulation

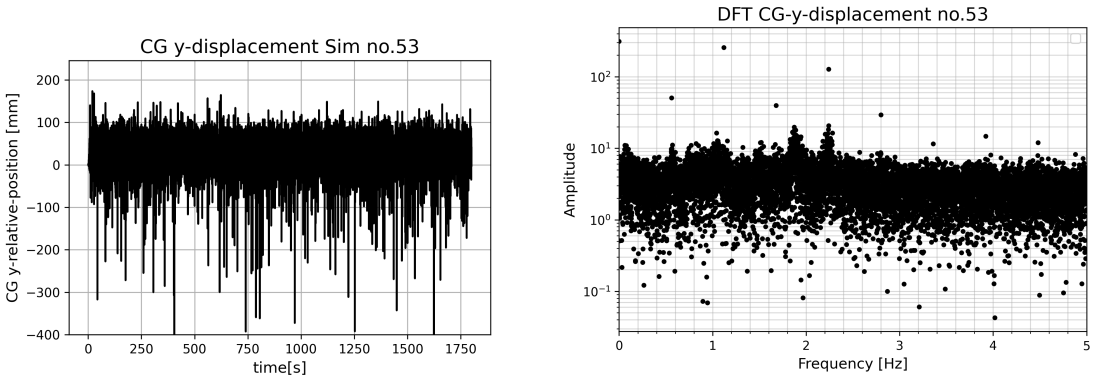

(a) Displacement of CG sim no.53 y-direction

(b) Fourier transofrm y-CG-displacement sim no. 53

Figure 6.11: Centre of gravity displacement y-direction chaotic simulation

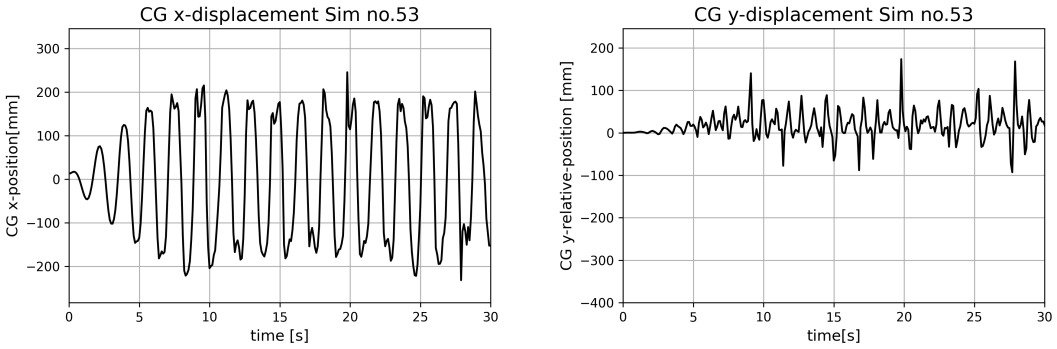

(a) Displacement of CG sim no. 53 x-direction

(b) Displacement of CG sim no. 53 y-direction

Figure 6.12: Closeup CG chaotic regime

6.1.3 Phase plane plot

One tool that shows in which regime is the system's response is the phase plot where the displacement of the free surface η/X_0 is plotted over the velocity of the free surface

$$\frac{1}{X_0\Omega}\frac{\dot{\eta}}{\partial t}$$

The velocity of the free surface was extracted from displacement data obtained from CFD using a forward finite difference scheme.

The shape of the plot gives information about the type of phenomenon and especially the effect of damping in the simulation. If the damping equals the inertial forces, it can be seen as a circular shape, instead, a more elliptical shape represents the presence of damping. This then demonstrates whether the mode is planar or chaotic in that once periodic-state conditions are reached in planar motion the damping is balanced with the inertia of the system, in chaotic motion there is a continuous loss of energy and thus the shape of the phase plot is more elliptical.

In figure 6.15 the phase plot shows the two simulations, as before simulation no. 42 and simulation no. 53, one which is known it be planar and another in a chaotic regime, the time considered is the last 20 seconds of both simulations.

Following observations from the height of the free surface, the plot for simulation no. 42 exhibits a mostly circular shape, while the second one shows irregularities suggesting the motion is not planar. By visualizing these plots, it is possible to qualitatively categorize the simulated cases as "fully planar" and "non-planar".

From these graphs, it is possible to extract a measure of circularity by calculating the variance of the distances between the points and the centroid of the pseudo-circular shape formed. In figure 6.16, the variance is reported as a function of the frequency dimensionless with the resonance frequency. It is evident that the closer the imposed frequency is to the resonance frequency, the higher the variance, indicating a non-planar region. To distinguish between the two regimes, a threshold value can be established, classifying all simulations with a variance below this threshold as planar.

From this consideration, figure 6.17 reports all the cases simulated where it is possible to observe the boundaries between the planar and chaotic test cases. In red is the line derived from the extrapolation of Miles' weakly non-linear theory, which marks the boundary between planar and chaotic simulations for an upright cylinder using the Eq. 2.5. We can see a slight discrepancy between the identification of the regime in the two geometries.
This graph for upright cylinders was reported by Ludwig [30] through values extracted from Miles [8][9] using weakly nonlinear theory.
To the best of our knowledge, this is the first plot of this nature applied to horizontal cylinders. While the figure was generated from purely numerical simulations,

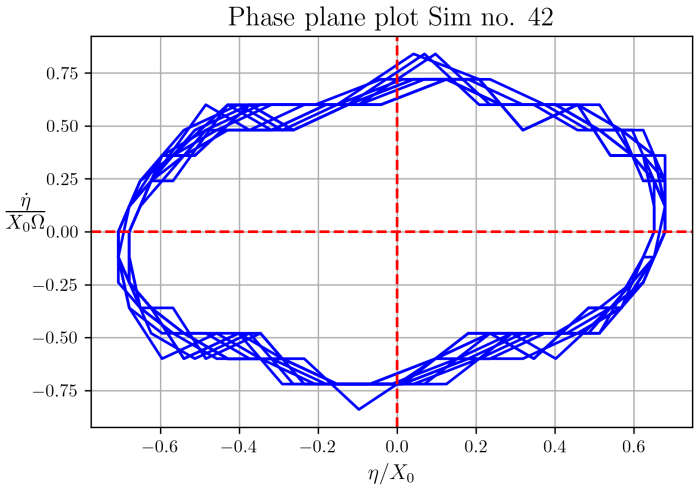

Figure 6.13: Phase plane plot Sim no. 42

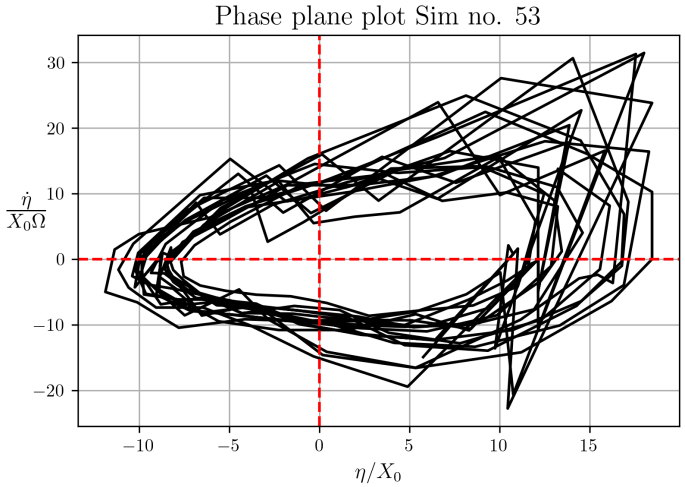

Figure 6.14: Phase plane plot Sim no. 53

Figure 6.15: Phase plane plots

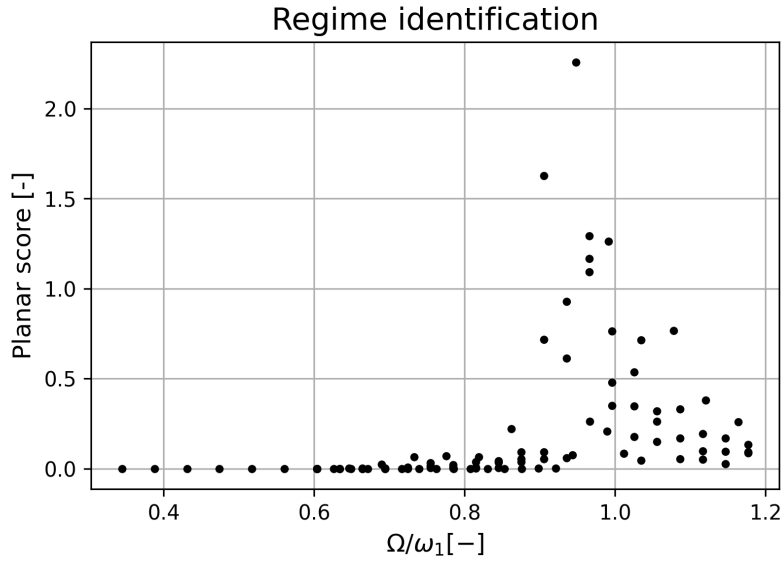

Figure 6.16: Regime Identification by circular score

yet to be validated experimentally, it provides a first approximation for the boundaries between these two sloshing wave regimes

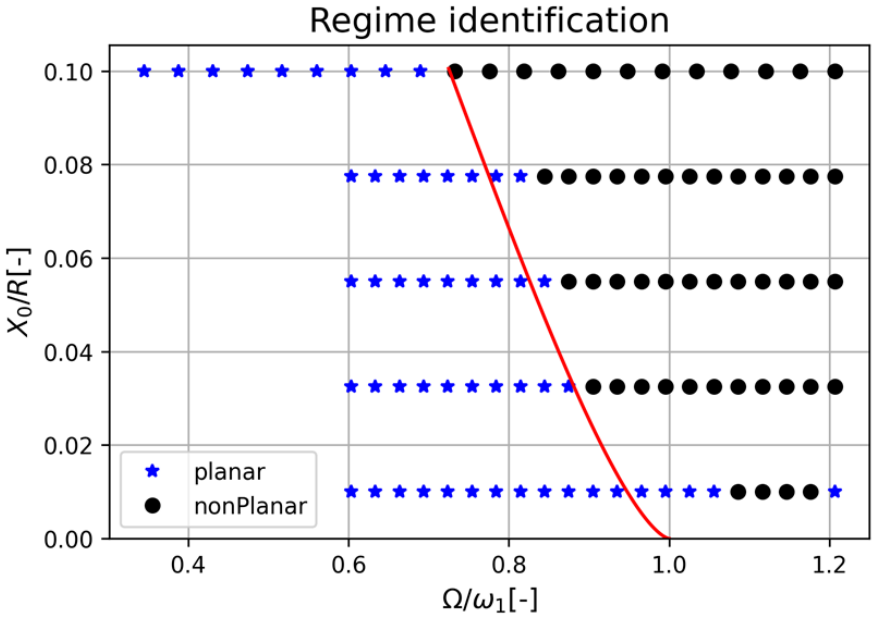

Figure 6.17: Regime Identification

Another option for determining the regime through phase plane plots is to go and evaluate the position of the centroid. It can be seen that the centroid is positioned very close to the origin of the axes (0,0) for planar simulations, it shifts in our case towards positive values in the case of chaotic simulations.

6.2 Damping evaluation

According to [18] and [17] the damping ratio in deep water condition ($h/R > 1$) is approximable with the follow equation

$$\zeta = 0.79\sqrt{\frac{\nu}{\sqrt{gR^3}}} \tag{6.1}$$

With this formulation, applying the definition of damping ratio, the constant damping coefficient for our case should be $\zeta = 0.00046911$. This value will then be compared with the values of the various CFD simulations and the damping values that are resolved by the optimizations.

Among the optimizers described in the previous chapter, the results below make a case for the Nelder-Mead optimizer. The other two optimizers: BFGS and the Stochastic Gradient Descent were used but set aside because the BFGS optimizer in optimizations that included all simulations tended to crash after a certain number of iterations, failing to converge and giving results that if evaluated would cause the cost function to explode. The stochastic solver works, the results converge but require a large number of iterations and a low learning rate, so since the optimizations were taking a long time, the N-M optimizer was used, which is faster and is also independent of initial values as shown through multiple restarts in the next section.

6.2.1 Performance of the potential flow model

Between the two reduced models that we explore in the theory part, the potential fluid model which consists of solving the differential equation 2.17 described in section 2.2, cannot quite identify the term damping. The main problem, that is possible to see in figure 6.18 is that there is a discrepancy between the solution at the beginning of the transient, the potential solution underestimates the height of the fluid, and the optimizer acting only on the damping coefficient cannot find an optimal solution even when optimizing for one simulation as in this case. This led to the exclusion of this model from the development of the reduced model in preference to the mechanical model which, as discussed below, succeeds through the sloshing mass parameter in achieving a good result on ROM performance

In spite of this, the potential fluid theory described in section 2.2.2 facilitates evaluation of the natural frequencies of the system. As seen in the Short-time Fourier transform and Discrete Fourier Transform figure 6.3 (b) and 6.4(b), the peaks depicted by the plots from the CFD simulation align precisely with the frequencies predicted by the potential theory.

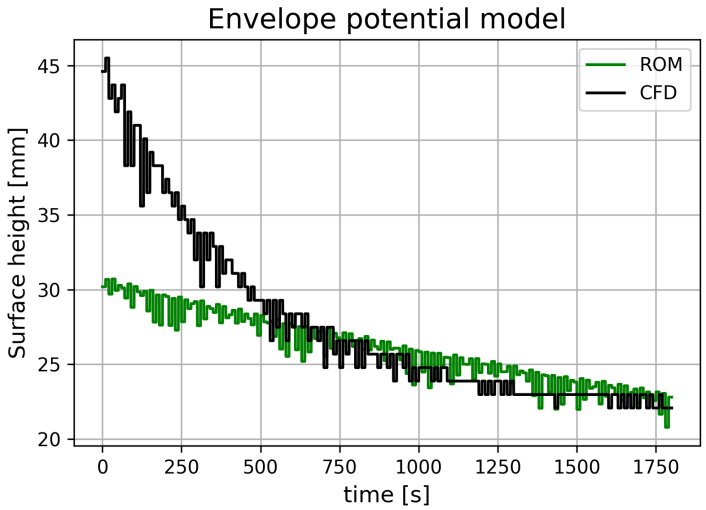

Figure 6.18: Optimization with potential solution

6.2.2 Performance of the mechanical model

In section 2.3, it is mentioned that for the mechanical model, the optimization parameters are defined as the damping coefficient ζ and the sloshing mass m_{sl} relative to the first resonance frequency, in the ways that will be discussed below.

By only considering the planar simulations and knowing that the model only gives the solution for wall displacement, it is assumed that the surface has a linear shape and interpolate the model's solution with the position of the probe at $\bar{r} = 0.75$ m. the displacement of the free surface as described equation 2.22 is multiplied by the evaluation radius (applying the linearity assumption)

$$\eta(t) = \frac{4m_{l|sl}x(t)}{\pi R^3 \rho}\bar{r}$$

Constant damping coefficient

$$\zeta = \text{const.}$$

The optimization is initially conducted on a single simulation, utilizing the simulation input values. Subsequently, the optimization is repeated taking all planar simulations into account in the cost function.

Figure 6.19 shows the envelope of the surface height at a fixed radius over time showing the CFD simulation and the result of the optimized model. o provide a clearer view, a zoom-in at the beginning and end of the simulation in figure 6.20 is also included.

The results that come out of this simulation are:

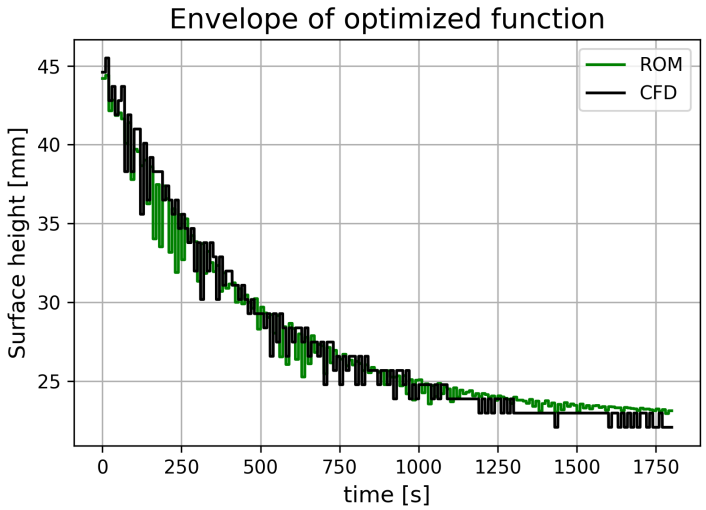

Figure 6.19: Envelope of surface height

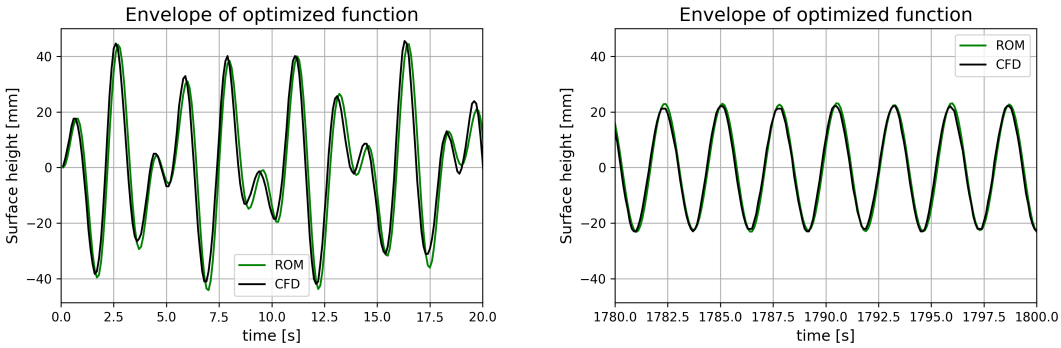

(a) Start of simulation

(b) End of simulation

Figure 6.20: Constant damping ROM

- $\zeta = 0.00062829$
- $m_{sl} = 0.687$

the result obtained for the damping coefficient is comparable with the result described in the literature which we find in Eq. 6.1, we can see that the results have the same order of magnitude, the value from the literature being about 30% lower than the value we found. This could be due to the fact that the geometries taken into consideration are different and that in our case the deep-water condition is not perfectly realized the reservoir is exactly half-filled. Furthermore, it is possible to state that for the horizontal cylinder, more liquid moving is in contact with the wall and therefore we expect there to be an increase in damping compared to the case of the vertical cylinder.

Optimizing for only one simulation finds a model that is in good agreement with the CFD results, both the point evolution of the signal and the envelope in the

transient are well predicted.

Starting from the results of the previous optimization, the process continues taking all planar simulations into account, which were chosen through sorting by phase plane plots.

As described in section 5.3, the cost function is defined as the sum of the cost functions of the individual simulation divided by the number of simulations.

The following parameters are found after the optimization processes considering all the planar simulations:

- $\zeta = 0.00060896$
- $m_{sl|1} = 0.7794$

The quality of the predictions of the model can be assessed through the cost function plotted over the Froude number relative to the simulation considered, which is shown in figure 6.22 while figure 6.21 shows the cost overall cost function over the iterations.

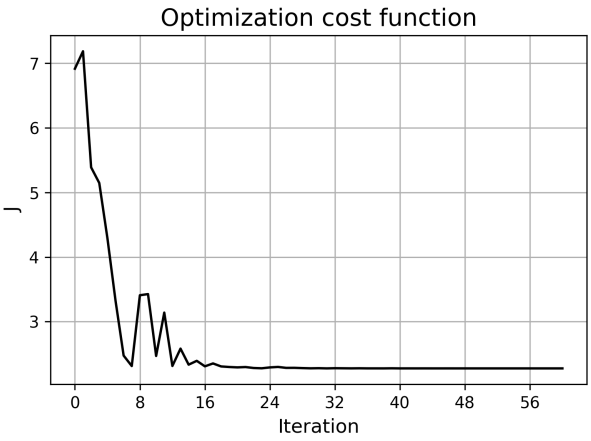

Figure 6.21: Overall cost function

the cost function, only considering the range of Froude inputs in the simulations has minima, when the Froude number is low, then when it's increased the model turns out to be unreliable, and the unreliability is not monotonically increasing as the number of Froude increases, so is difficult to have a wide range of applicability of the model.

The results of the model that optimizes all simulations were used to evaluate simulation no. 42 that had been optimized earlier. The model in this case overestimates the sloshing mass that has increased, figure 6.23.

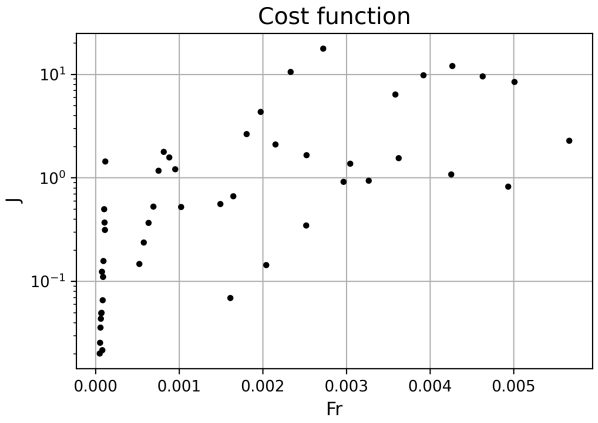

Figure 6.22: Cost function of each simulation

It is possible to conclude that estimating the constant sloshing mass constant in all simulations is an error and that as the damping coefficient should at least be a function of the Froude number.

In figures 6.23 and 6.24, it is observed that, unlike the previous case where only one simulation was optimized, an error exists between the two estimations. Notably, the envelope highlights a discrepancy between the CFD results and the model results.

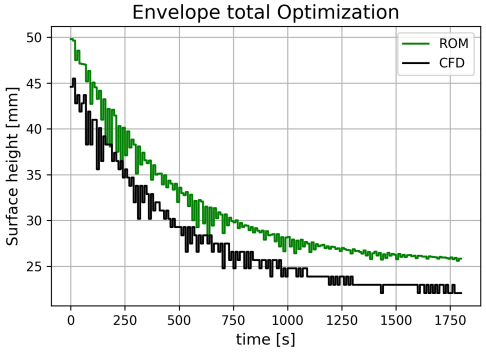

Figure 6.23: Envelope Reassessment of simulation with the new parameters

In the quest to identify the minima within that define the optimization problem, the strategy of employing multiple restarts is a robust technique that enhances the efficacy of the search process. Initiating the optimization algorithm from various starting points can increase the probability of circumventing local minima, thereby facilitating the discovery of the global minimum. The starting points were choosed by taking random values in the range centered in the derived optimum value and two orders of magnitude wide. Each restart acts as an independent trial, exploring the solution space from a different vantage point.

Multiple restarts were performed by considering the total optimization and going

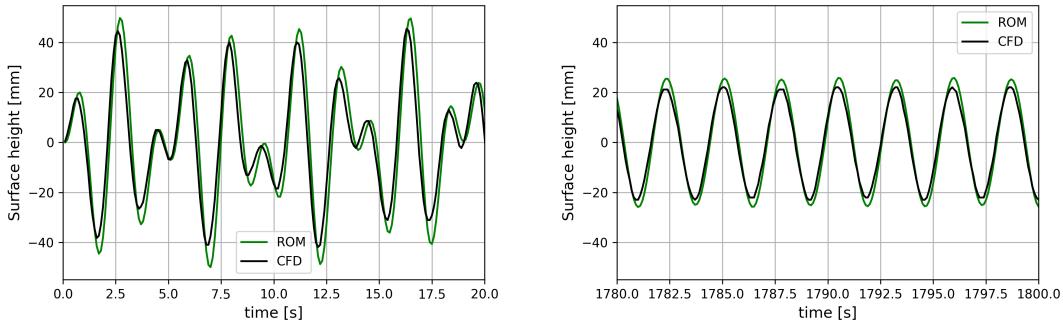

(a) Start of simulation (b) End of simulation

Figure 6.24: Reassessment of simulation with the new parameters

to evaluate the 2 parameters after a set number of iterations. In figure 6.25 is evaluated the result of multiple optimizations as a function of the restart.

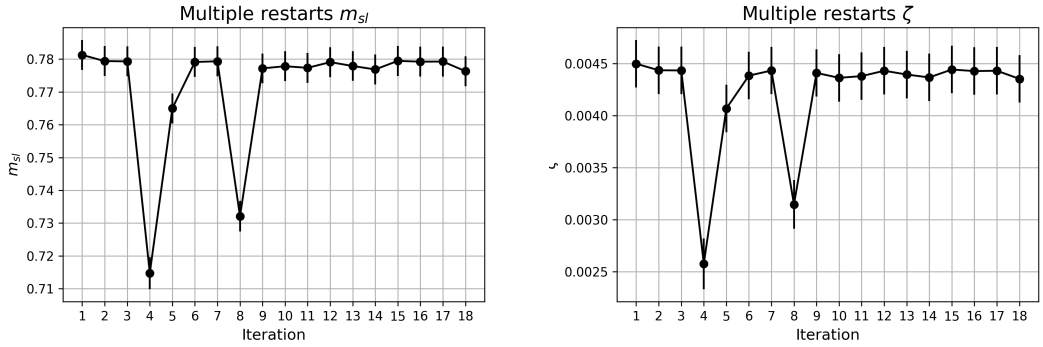

Figure 6.25: Multiple restarts

It can be seen that after all optimizations the results obtained tend to converge to the same value for the two parameters considered it is therefore shown that the optimizer has reached a minimum which can be considered global.

Non-constant damping coefficient Damping coefficient

$$\zeta = f(\mathrm{Re}(t), \mathrm{Fr})$$

The second approach used is to express the damping coefficient ζ as a parametric function of the state of the system and the forcing conditions. The simulation dependence is expressed by the Froude number defined:

$$Fr = \frac{(X_0\Omega)^2}{gR}$$

instead, the velocity dependence is done using the Reynolds defined on the vertical velocity of the surface, extracted by deriving in time the displacement signal

already processed,

$$Re(t) = \frac{u^*(t)R}{\nu}$$

where with finite differences forward of the first-order is used to extract the velocity of the free surface

$$u^*(t_i) = \frac{\partial \eta(t_{i-1})}{\partial t}$$

The damping coefficient is finally defined in the form:

$$\zeta = a \ \mathrm{Fr}^b \left(\frac{\mathrm{Re}}{Re_{cr}} \right)^c$$

Where parameters a, b and c are the optimization parameters, as well as the sloshing mass.

As in the previous section, the same method is employed, starting with optimization for one simulation before proceeding to create a total optimization considering all planar simulations.

Figure 6.26 shows the cost function for the total optimization as a function of iterations and figure 6.27 shows the evaluation of the cost function for each simulation, which is shown as a function of the number of Froude that characterizes the single simulation.

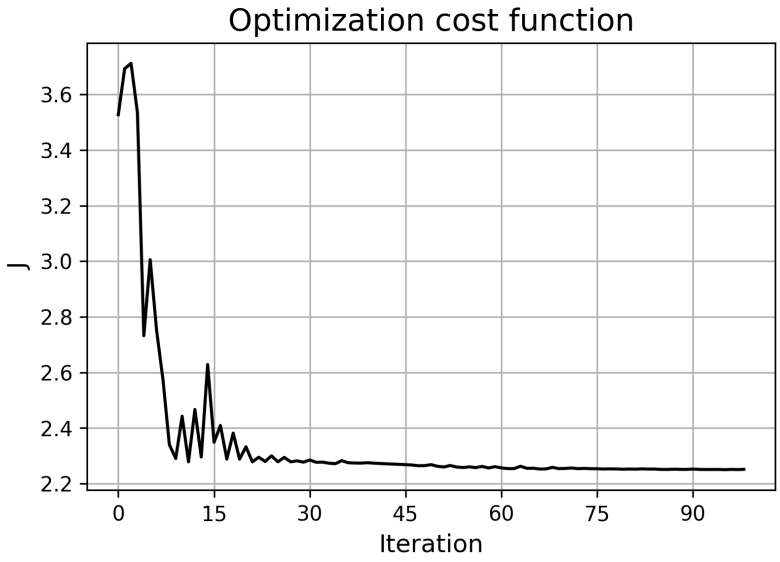

Figure 6.26: Overall cost function

the parameter values derived from the total optimization are:

- $a = 0.0023$

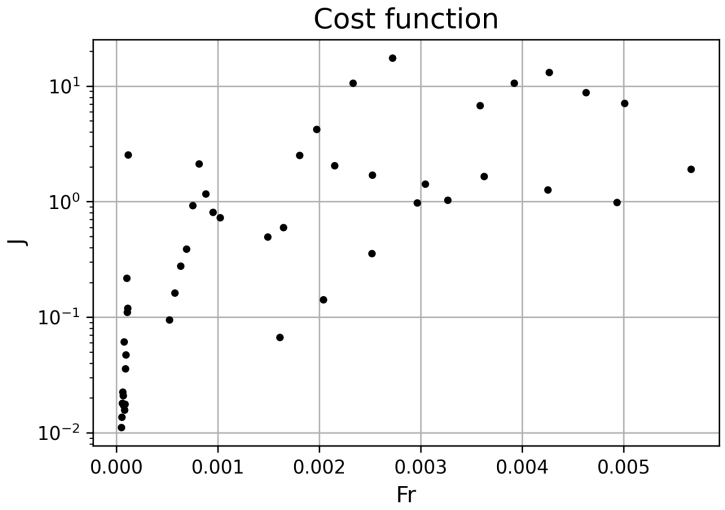

Figure 6.27: Cost function of each simulation

- $b = -0.0992$
- $c = 0.0064$
- $m_{sl} = 0.7785$

Finally, figure 6.28 displays the envelope of simulation no. 42 with the damping coefficient as a function of time. It is observed that there is similar behavior to considering constant damping. By optimizing for all simulations, achieving a very good result for individual simulations proves challenging. From the figure 6.29 it

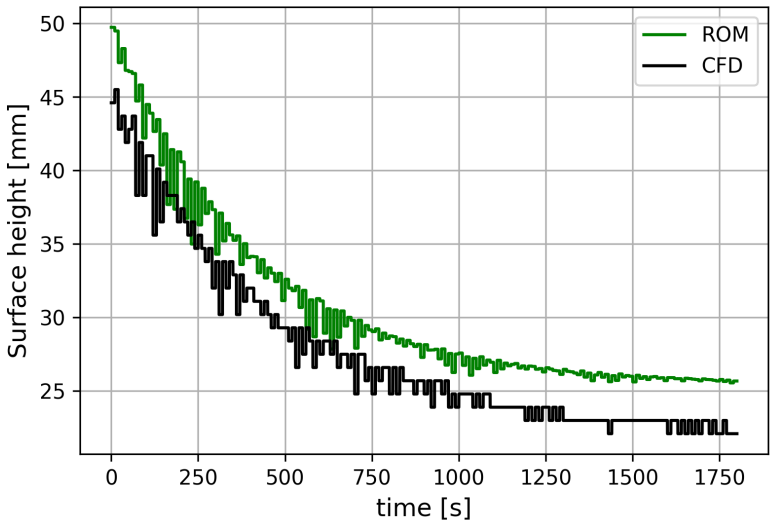

Figure 6.28: Envelope of the simulation no. 42

is possible to visualize an average of the damping coefficient as a function of time, as is to be expected this decreases as in the initial transient there is more mass movement and the velocities involved are higher than in the final periodic regime, in which the fluid is only moved at the frequency imposed by the forcing.

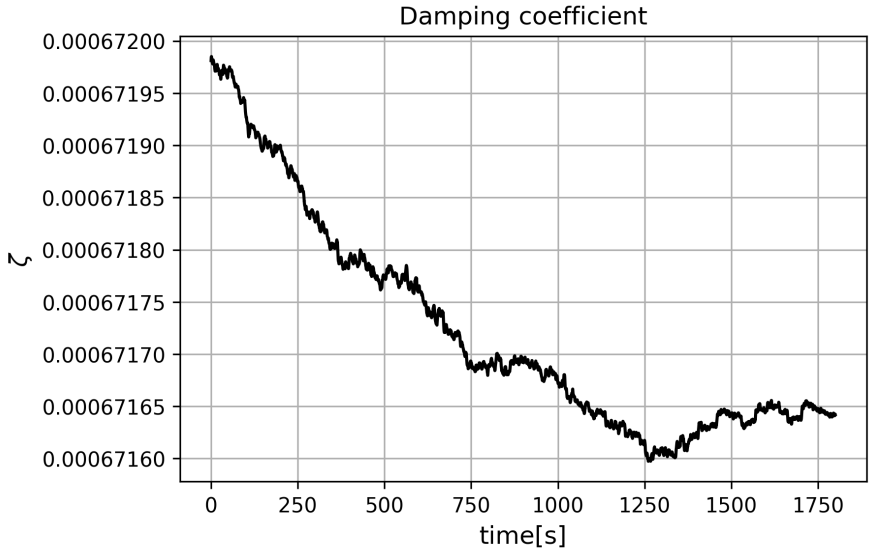

Figure 6.29: Variable damping

6.2.3 Comparison between the two models

In this last section, is evaluating the performance of the two models, the first considering constant damping and the second considering variable damping by viewing the cost functions in figure 6.30. From the graph, it can be concluded that the model where $\zeta = f(Re, Fr)$ is superior because it yields lower values of the cost function, indicating minimal deviation from CFD simulations. From the same graph, we can see that the more we increase the Froude number and the closer we get to the resonance frequency, the more the model fails.

In both approaches, an increase in error is observed as the number of Froude increases.

Finally, we wanted to evaluate how the 2 models used behave and compare them with literature values and numerical simulations. In table 6.1 data from 3 simulations, with increasing Fr are reported. with the increasing of the Froude number we can see that also the cost function J is increasing demonstrating a loss of reliability of the model. We can see that for all three simulations considered, the lowest cost function turns out to be the one expressing damping as the parametric function described above.

With the same definition of damping, we find that by increasing the Froude num-

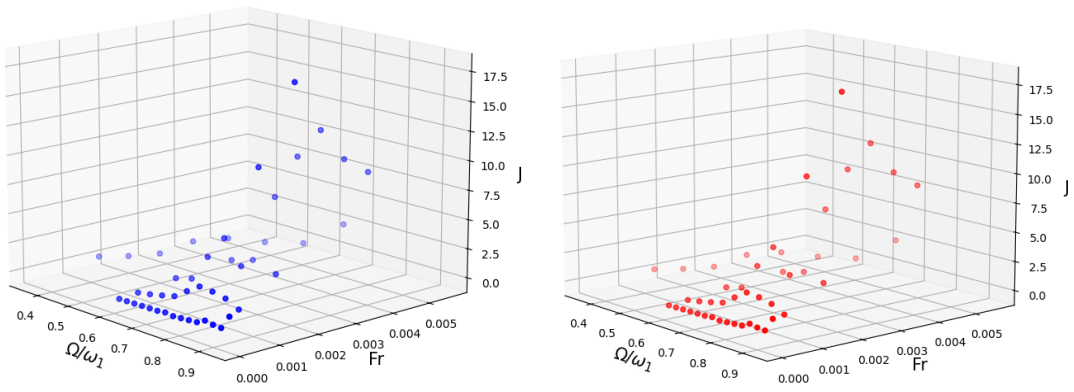

(a) Cost function for constant damping (b) Cost function for variable damping

Figure 6.30: Comparison between the two models

Table 6.1: ROM compared

ID	X_0	Ω	Ω/ω_1	**Fr**	**J Literature**	**J constant**	**J variable**
10	0.01	2.943	0.81	8.84E-05	0.286	0.115	0.043
42	0.033	2.309	0.63	0.000575	0.311	0.241	0.179
87	0.078	2.859	0.78	0.00501	67.45	8.344	6.444

ber, the cost function increases. This increment of the cost function can be explained as a more non-linear behaviour in that there is increasing the Froude number or it is due to the fact that the damping formulation are missing other terms.

The findings derived from the table 6.1 are further displayed by figures 6.31 and 6.32, we can see the envelopes of the simulations compared with the literature value of damping and sloshing mass and the optimization functions.

It is also analyzed the possibility of using the reduced model for the simulations not taking into account to train the model, which are the chaotic regime simulations.
Table 6.2 reports the average of the cost function for each damping model utilized considering first only all the planar simulations and then only the chaotic simulations.

The average of the cost function increases by around two orders of magnitude and the model is, therefore, no longer reliable.

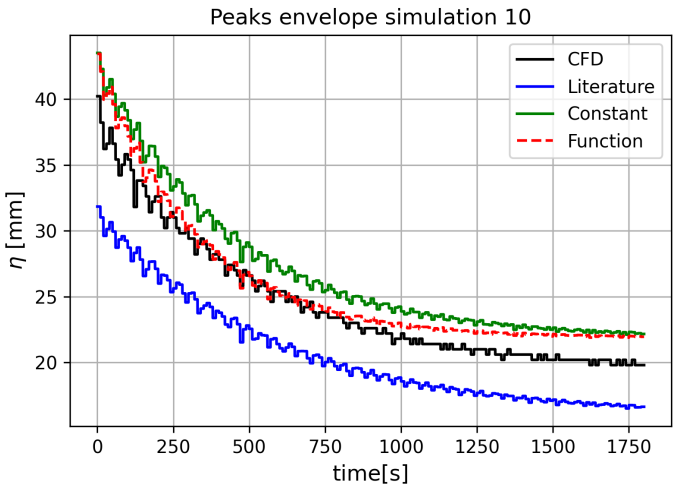

(a) Envelope surface height simulation ID 10

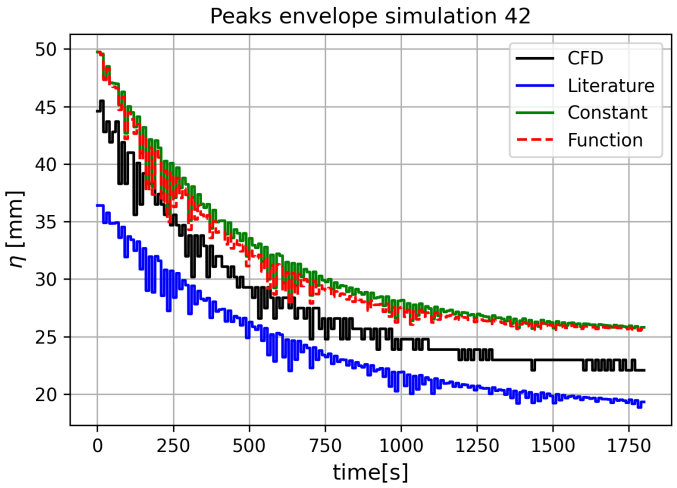

(b) Envelope surface height simulation ID 42

Figure 6.31: Envelope of surface height simulations ID 10 and 42

Table 6.2: ROM extended to chaotic cases

Approach	Average J in planar case	Averege J non Planar cases
Literature	7.81	200.04
Constant	2.27	174.5
Function	2.25	193

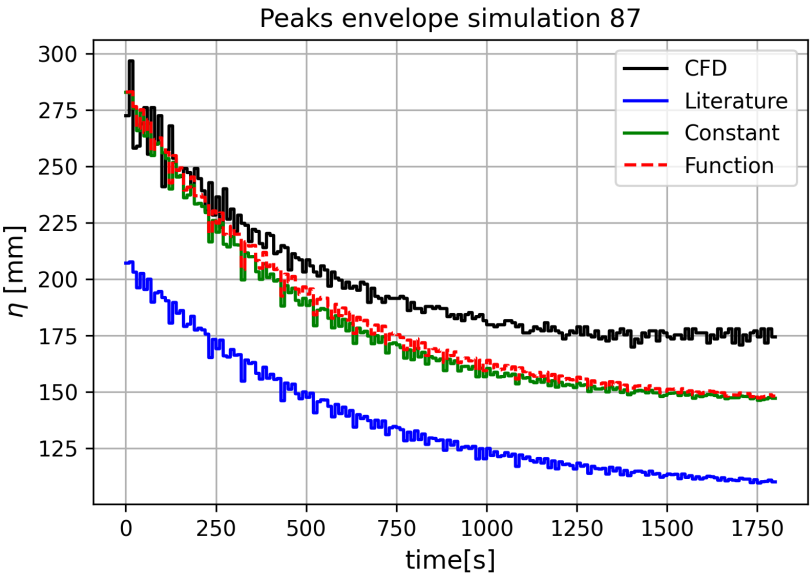

Figure 6.32: Envelope of surface height simulation ID 87

Chapter 7

Conclusions

The result of this work can be summarised in two main findings:
The first is the identification of the sloshing regime for a horizontal cylinder as a function of the amplitude and frequency of the imposed displacement. From the literature review carried out, this is the first time such a phase diagram has been derived from a horizontal cylindrical tank undergoing transverse excitation sloshing. It is possible to visualize the boundaries for the planar and chaotic regimes not yet analyzed in detail by existing theories such as the weakly non-linear theory already mentioned several times [8] described by Miles.
The second is to evaluate the possibility of introducing a reduced order model to visualize the displacement of the liquid surface in the planar regime, which works in a certain range of Froude numbers.

The combination of the two results produces a simplified model capable of predicting the sloshing dynamics in isothermal conditions, where therefore the thermodynamic component of the system is neglected. This would lead to the creation of a surrogate model that from input signals of displacement and frequency would create a real-time prediction of the displacement for a future implementation to control the sloshing within the tank to dampen the oscillations that bring several criticalities to the system.

7.1 Future work

Continuing with the considered case of a half-filled cylinder, other types of valid functions for the damping coefficient and sloshing mass could be analysed. In addition, it will be useful to analyse a more homogeneous range of Froude input values by considering the planar region of the graph described in figure 6.17 in order to have a higher number of different Fr and to calibrate the reduced model with this data.

Since the simulations used assume that the tank is half-filled, part of the future work will be to analyse different tank-filling rates in order to assess whether the damping solutions used in this work are still valid in those cases. There are other resonance frequencies to take into account such as the sloshing mass predicted by the theory changes but the relationship for the damping coefficient could remain the same perhaps also considering the resonance frequency related to the percentage of filling the tank.

Another consideration on the movement of the centre of gravity, even in the chaotic regime, it presents a symmetry in response, taking this data into account will certainly be a plus for the identification of the reduced system.
In addition, predicting the position of the centre of gravity with a reduced system would lead to future implications in the engineering plan as one could put a system of tank movement in counter-phase that would dampen the oscillations due to the sloshing of the liquid inside the tank.

Finally, given that cryogenic fluids are generally used in tanks of this kind as fuel transport, it is certainly a step to take to assess the implications of a non-isothermal model of the system. At this stage, there is also the component of phase change of the liquid, typically cryogenic, which also damages the pressure inside the tank. The search for a possible relationship between damping under isothermal conditions with a model that takes into account the thermodynamics of the system is suggested.

Appendices

Appendix A

OpenFoam algorithms

The algorithm utilized by the solver is PIMPLE, which combines the PISO (Pressure-Implicit with Splitting of Operators) and SIMPLE (Semi-Implicit Method for Pressure Linked Equations) algorithms.

- Solve the Momentum Equation: Update the velocity field by solving the momentum equation, including the pressure gradient term. The α equation is solved with the MULES scheme.
- Pressure Correction Equation: Compute corrections to the pressure field to ensure mass conservation, a step that's iterated to refine both pressure and velocity fields towards divergence-free conditions.
- Update Velocity and Pressure Fields: Apply the pressure corrections to update the velocity and pressure fields, ensuring that the continuity equation is satisfied.

In particular the interFoam solver use for two-liquid VOF method is described in [31]:

1. Initial data
2. $t = t + \Delta t$
3. Adjustment of the time step according to maximum Courant number
    - START: Iteration over the PIMPLE Loop
    - Solving the α equation by VOF and MULES (Multidimensional Universal Limiter with Explicit Solution)
    - Calculations of mixture properties (ρ,α, σ)
    - PISO Loop over pressure equation

- Indicator of Error
- END: Iteration over the PIMPLE Loop
- Calculations of the turbulence properties

A.1 Modified interFoam solver

InterFoam solver present in OpenFoam does not allow the specify a variable acceleration field with time. It is present a constant acceleration field, that is usually used to model the gravity acceleration.

As described in chapter 4, a variable acceleration allows the sloshings phenomenon to be simulated without using mesh motion, which has a considerable computational cost as seen in 4.3.1. The modified interFoam solver source code that allows for a variable acceleration field, called interDispFoam is presented below. in the parts where the code varies from the initial source. This code is valid for version v2206, it may have some variations in the way variables and fields are called in other versions of openFOAM.

The following code is a modified version of the interFoam.C file in the solver folder:

```
*---------------------------------------------------------------------------*\
  =========                 |
  \\      /  F ield         | OpenFOAM: The Open Source
                              CFD Toolbox
   \\    /   O peration     |
    \\  /    A nd           | www.openfoam.com
     \\/     M anipulation  |
-------------------------------------------------------------------------------
```

```
[...]
    int main(int argc, char *argv[])
    {
    #include "postProcess.H"
    #include "setRootCaseLists.H"
    #include "createTime.H"
[...]
IOdictionary ioAccelDict(
    IOobject(
        "accelerationDict", // dictionary name
        runTime.constant(),  // dict is found in "constant"
        mesh,                // registry for the dict
        IOobject::MUST_READ, // must exist, otherwise failure
        IOobject::NO_WRITE   // dict is only read by the solver
    )
);
// Read the acceleration dictionary
dictionary accelerationDict(ioAccelDict);

word accelerationCoeffs = "accelerationCoeffs";
word gravityAcceleration = "gravityAcceleration";

// Access the subdictionary "accelerationCoeffs"
const dictionary& subDict =
        accelerationDict.subDict(accelerationCoeffs);
vector amplitudeAcc;
vector omegaAcc;
```

```
if (subDict.readIfPresent("amplitude", amplitudeAcc) &&
    subDict.readIfPresent("omega", omegaAcc)) {
    Info << "Acceleration amplitude [m] = " << amplitudeAcc
        << endl;
    Info << "Acceleration omega [rad/s] = " << omegaAcc << endl;
} else {
    Info << "Values 'amplitude' and 'omega' not found in
        the subdictionary." << endl;
}

// Access the subdictionary "gravityAcceleration"
const dictionary& gravityDict = accelerationDict.subDict(gravityAcceleration);
vector gravityAcc;

if (gravityDict.readIfPresent("gravity", gravityAcc)) {
    Info << "Gravity acceleration [m/s2] = " << gravityAcc << endl;
} else {
    Info << "Value 'gravity' not found in the subdictionary." << endl;
}
// End of acceleration dictionary reading
// * * * * * * * * * * * * * * * * * * * * * * * * * * * * * * * * * * * * //
    Info<< "\nStarting time loop\n" << endl;

    while (runTime.run())

[...]

/Current acceleration field vector (Harmonic oscillation
   // + constant value) for the 3 components
const dimensionedScalar gunits ("gunits", dimensionSet(0,1,-2,0,0,0,0),1);

Foam::dimensioned<Foam::Vector<double>> grav=gunits*amplitudeAcc[0]*
    Foam::pow(omegaAcc[0],2)*Foam::cos(omegaAcc[0]*runTime.value())
    *Foam::vector(1,0,0)+gunits*gravityAcc[0]*Foam::vector(1,0,0)+

        gunits*amplitudeAcc[1]*Foam::pow(omegaAcc[1],2)*
    Foam::cos(omegaAcc[1]*runTime.value())*Foam::vector(0,1,0)+
        gunits*gravityAcc[1]*Foam::vector(0,1,0)+

        gunits*amplitudeAcc[2]*Foam::pow(omegaAcc[2],2)
 *Foam::cos(omegaAcc[2]*runTime.value())*Foam::vector(0,0,1)+
        gunits*gravityAcc[2]*Foam::vector(0,0,1);


Info << " Current Gravity @ t=" << runTime.timeName ()
                << ": (g_x g_y g_z) = (" << grav.component(vector::X).value()
                << " " << grav.component(vector::Y).value()
                << " " << grav.component(vector::Z).value()
                << ")"
                << endl;
Info<< "Calculating field g.h\n" << endl;
volScalarField gh("gh", grav & mesh.C());
surfaceScalarField ghf("ghf", grav & mesh.Cf());
// ---- Pressure-velocity PIMPLE corrector loop
        while (pimple.loop())
```

```
        {
[...]
Info<< "End\n" << endl;

    return 0;
}
```

The new dictionary into which we enter the amplitude and frequency of the forcing is `accelerationDict`, should be placed in the folder `costant` of our simulation folder and is presented as follow:

```
    /*--------------------------------*- C++ -*----------------------------------*/
| =========                 |                                                 |
| \\      / F ield          | OpenFOAM: The Open Source CFD Toolbox           |
| \\    / O peration        | Version: v2206.0                                |
| \\  / A nd                | Web: www.OpenFOAM.org                           |
| \\/ M anipulation         |                                                 |
\*---------------------------------------------------------------------------*/
FoamFile
{
        version 1.0;
        format ascii;
        class dictionary;
        location "constant";
        object accelerationDict;
}
// * * * * * * * * * * * * * * * * * * * * * * * * * * * * * * * * * * * * * //

accelerationCoeffs
{
        amplitude (0.0325 0 0); // amplitude of the acceleration
        omega (4.75 0 0); // frequency of the acceleration
}
gravityAcceleration
{
        gravity (0 -9.81 0);
}
```

Bibliography

[1] S. Papaspyrou, S.A. Karamanos, and D. Valougeorgis. Response of half–full horizontal cylinders under transverse excitation. *Journal of Fluids and Structures*, 19:985–1003, 08 2004.

[2] Alessia Simonini. *Sloshing dynamics investigation by means of non-intrusive measurement techniques*. PhD thesis, 2018.

[3] Andr ´e Da Luz Moreira. *Comparison between CFD and experimental results of the sloshing rising wave in a microgravity environment*. PhD thesis, 2019.

[4] Raouf A Ibrahim. *Liquid sloshing dynamics : theory and applications*. Cambridge University Press, 2006.

[5] H. C. Mayer and R. Krechetnikov. Walking with coffee: Why does it spill? *Physical Review E*, 85, 04 2012.

[6] H.N. Abramson. The dynamic behavior of liquids in moving containers, with applications to space vehicle technology. *NASA*, 1966.

[7] Balaji Sivasubramanian, Leander V Paul, Sanjay Krishnappa, and Sathya N Gangadharan. A hybrid magneto-active propellant management device for active slosh damping in spacecraft. *56th AIAA/ASCE/AHS/ASC Structures, Structural Dynamics, and Materials Conference*, 01 2015.

[8] John W. Miles. Internally resonant surface waves in a circular cylinder. *Journal of Fluid Mechanics*, 149:1, 12 1984.

[9] John W. Miles. Resonantly forced surface waves in a circular cylinder. *Journal of Fluid Mechanics*, 149:15, 12 1984.

[10] Franklin Dodge and H Abramson. Liquid propellant dynamics in the saturn/apollo vehicles - a look back. 04 2000.

[11] Brian Bjelde, Max Vozoff, and Gwynne Shotwell. The falcon 1 launch vehicle: Demonstration flights, status, manifest, and upgrade path. 01 2007.

[12] Arnold Van Foreest. Modeling of cryogenic sloshing including heat and mass transfer. *46th AIAA/ASME/SAE/ASEE Joint Propulsion Conference amp; Exhibit*, 07 2010.

[13] Jeswin Joseph, Gagan Agrawal, Deepak Kumar Agarwal, J.C. Pisharady, and S. Sunil Kumar. Effect of insulation thickness on pressure evolution and thermal stratification in a cryogenic tank. *Applied Thermal Engineering*, 111:1629–1639, 01 2017.

[14] Matthew E Moran, Nancy B Mcnelis, Maureen T Kudlac, Mark S Haberbusch, and George A Satornino. Experimental results of hydrogen slosh in a 62 cubic foot (1750 liter) tank. *Joint Propulsion Conference*, pages 27–29, 06 1994.

[15] T. Arndt. *Sloshing of Cryogenic Liquids in a Cylindrical Tank under normal Gravity Conditions*. PhD thesis, 2011.

[16] Chin S. Lin, Neil T. Van Dresar, and Mohammad M. Hasan. Pressure control analysis of cryogenic storage systems. *Journal of Propulsion and Power*, 20:480–485, 05 2004.

[17] Hong Yang, Ravi Purandare, John Peugeot, and Jeff West. Prediction of liquid slosh damping using a high resolution cfd tool. *48th AIAA/ASME/SAE/ASEE Joint Propulsion Conference Exhibit*, 07 2012.

[18] David G. Stephens, Leonard H. Wayne, and Tom W. Perry Jr. Investigation of the damping of liquids in right-circular tanks, including the effects of a time-variant liquid depth, 07 1962.

[19] Lazaros A Patkas and Spyros A Karamanos. Variational solutions for externally induced sloshing in horizontal-cylindrical and spherical vessels. 133:641–655, 06 2007.

[20] Luca Guagliumi, Alessandro Berti, Eros Monti, and Marco Carricato. A simple model-based method for sloshing estimation in liquid transfer in automatic machines. *IEEE Access*, 9:129347–129357, 01 2021.

[21] Thomas A. Lance. Analysis of propellant slosh dynamics and generation of an equivalent mechanical model for use in preliminar voyager autopilot design studies, 12 1966.

[22] Stephen J. Kline and J. R. Radbill. Similitude and approximation theory. *Journal of Applied Mechanics*, 33:238–238, 03 1966.

[23] M.C. Ruzicka. On dimensionless numbers. *Chemical Engineering Research and Design*, 86:835–868, 08 2008.

[24] Chris Greenshields. Openfoam v11 user guide, 07 2023.

[25] C.W Hirt and B.D Nichols. Volume of fluid (vof) method for the dynamics of free boundaries. *Journal of Computational Physics*, 39:201–225, 01 1981.

[26] Changfang Zou, Deyu Wang, and Zhonghua Cai. Effects of boundary layer and liquid viscosity and compressible air on sloshing characteristics. 7:670–690, 07 2015.

[27] Benjamin C Kuo and Farid Golnaraghi. *Automatic Control Systems*. 2003.

[28] Jorge Nocedal and Stephen J Wright. *Numerical optimization*. Springer, 2006.

[29] J. A. Nelder and R. Mead. A simplex method for function minimization. *The Computer Journal*, 7:308–313, 01 1965.

[30] C. Ludwig, M.E. Dreyer, and E.J. Hopfinger. Pressure variations in a cryogenic liquid storage tank subjected to periodic excitations. *International Journal of Heat and Mass Transfer*, 66:223–234, 11 2013.

[31] Le-Quyen Nguyen-Thi, Viet-Dung Nguyen, Xavier Pierens, and Patrice Coorevits. An experimental and numerical study of the influence of viscosity on the behavior of dam-break flow. *Theoretical and Computational Fluid Dynamics*, 35:345–362, 02 2021.